Advances in Industrial and Manufacturing Engineering 7 (2023) 100128

Contents lists available at ScienceDirect

Advances in Industrial and Manufacturing Engineering

journal homepage: www.elsevier.com/locate/aime

Regular aricles

Effect of uncertainty of material parameters on stress triaxiality and Lode angle in finite elasto-plasticity—A variance-based global sensitivity analysis

M. Böddecker [a], M.G.R. Faes [b], A. Menzel [a,c], M.A. Valdebenito [b,*]

[a] TU Dortmund University, Institute of Mechanics, Leonhard-Euler-Str. 5, Dortmund, 44227, Germany
[b] TU Dortmund University, Chair for Reliability Engineering, Leonhard-Euler-Str. 5, Dortmund, 44227, Germany
[c] Lund University, Division of Solid Mechanics, P.O. Box 118, Lund, SE-221 00, Sweden

ARTICLE INFO

Keywords:
Uncertainty
Probability
Finite elements
Material parameters
Finite elastoplasticity
Stress triaxiality
Lode angle
Sensitivity
Gaussian process

ABSTRACT

This work establishes a computational framework for the quantification of the effect of uncertainty of material model parameters on extremal stress triaxiality and Lode angle values in plastically deformed devices, whereby stress triaxiality and Lode angle are accepted as key indicators for damage initiation in metal forming processes. Attention is paid to components, the material response of which can be represented as elasto-plastic with proportional hardening as a prototype model, whereby the finite element method is used as a simulation approach generally suitable for complex geometries and loading conditions. Uncertainty about material parameters is characterized resorting to probability theory. The effects of material parameter uncertainty on stress triaxiality and Lode angle are quantified by means of a variance-based global sensitivity analysis. Such sensitivity analysis is most useful for apportioning the variance of the stress triaxiality and Lode angle to the uncertainty on material properties. The practical implementation of this sensitivity analysis is carried out resorting to a Gaussian process regression, Bayesian probabilistic integration and active learning in order to decrease the associated numerical costs. An example illustrates the proposed framework, revealing that parameters governing plasticity affect stress triaxiality and Lode angle the most.

1. Introduction

Forming processes of metals are of the highest importance in industrial and manufacturing engineering. Such processes affect material properties along the respective load paths, in particular in view of deformation-induced damage effects. These effects, together with initial material properties, influence, amongst others, performance and lifetime properties of related components. The prediction of properties at material and component level is typically based on advanced modeling and simulation approaches; see, e.g., Banabic (2010) and Sprave et al. (2020) as well as references cited therein. In general however, loading conditions, geometry and initial material properties are associated with uncertainties due to inherent variabilities, insufficiency in the available information, or a combination of both Faes et al. (2021). In this work, a simulation framework is established to analyze uncertainties related to initial material properties, respectively material parameters of the underlying material model. In particular, their influences on measures used to detect damage effects are of interest here. This approach ultimately contributes to constructing a simulation framework that allows to optimize the robustness of metal forming processes to variations in material and manufacturing parameters by explicitly quantifying the effect of uncertain or variable quantities on the overall damage state of the formed metal part.

Stress triaxiality – as a ratio that relates hydrostatic stress to a shape changing related deviatoric stress contribution – is accepted as one of the key indicators for quantifying damage initiation (and evolution) in metal forming processes of mechanical components; see the elaborations and models for (ductile) damage discussed in, e.g., Lemaitre (1996) and Murakami (2012), and related models proposed for non-local ductile damage in Mediavilla et al. (2006) and Zhu and Engelhardt (2018). In addition to stress triaxiality, the Lode angle, which can be considered as the orientation of the stress state within its octahedral plane in principal stress space, is established as a stress measure relevant for the initiation (and evolution) of damage related phenomena, in particular at states of low stress triaxiality; cf. Bai and Wierzbicki (2008) and the investigations including finite element analysis (Malcher et al., 2012; Malcher and Mamiya, 2014; Darlet and Desmorat, 2015). Moreover, the effect of the respective stress state on both, damage initiation and evolution is elaborated in Brünig et al. (2013) with focus of different damage mechanisms depending of stress triaxiality, Lode angle and stress intensity.

* Corresponding author.
E-mail address: marcos.valdebenito@tu-dortmund.de (M.A. Valdebenito).

https://doi.org/10.1016/j.aime.2023.100128
Received 27 March 2023; Received in revised form 14 July 2023; Accepted 3 September 2023
Available online 9 September 2023

Stresses cannot be directly measured in experiments, but (typically) forces and displacements can. At homogeneous states of deformation, stresses can then be calculated directly from measured force levels and information of, e.g., cross-sectional area. In general, stresses are computed based on suitable numerical methods, such as the finite element method, in combination with a constitutive, respectively material model. In consequence, particular values of stress triaxiality and Lode angle in general depend, amongst other factors, on the particular constitutive model and the particular material properties associated with a specific component under consideration. Solving the related finite element model is usually a challenging task from a numerical viewpoint, as it may comprise a large number of degrees of freedom and may demand repeated iterations to capture nonlinear material behavior.

In summary, stress triaxiality and Lode angle are responses, respectively measures of interest, which are dependent on material properties. In practice, selecting suitable values for material parameters of a model reflecting the respective material properties may be challenging due to uncertainty associated with these, such as variability of raw materials or production processes, to name but a few; see, e.g., Oakley et al. (1998). A possible means for capturing uncertainty regarding material parameters consists of applying probability theory (see e.g., Fishman (1996)). Indeed, the uncertainty about parameters can be described in terms of random variables with a probability distribution. The type of probability distribution (for example, Normal, uniform, etc.) and its distribution parameters (for example, mean, variance) can be selected based on prior knowledge combined with experimental measurements. Following probability theory as described previously, the (predicted) measure of interest (either stress triaxiality or Lode angle) is no longer a fixed, crisp value but instead, it becomes a random variable itself. However, its probability distribution and distribution parameters are usually different from those prescribed to the material parameters. In fact, recall that the measure of interest is calculated based on, e.g., a finite element analysis which is nonlinear in its degrees of freedom and, moreover, the material model itself may also be nonlinear in its material parameters. Hence, even if uncertainty regarding material parameters can be quantified by means of probability distributions, it is still a challenge to characterize the resulting uncertainty on the measure of interest, as there is no closed-form access to its probabilistic characteristics. Hence, when quantifying uncertainty of this measure, one must focus on specific probabilistic descriptors, such as second-order statistics (that is, mean and variance), confidence intervals or probabilities of exceeding a critical value, to name a few.

One probabilistic calculation which is very informative in practice is the variance-based global sensitivity analysis, which produces the so-called Sobol' indices (Sobol', 1993). In a nutshell, Sobol' indices explain which part of the variance of the measure of interest can be attributed to the uncertainty (described here using the variance) associated with the input parameters of a certain model. In the case of this work, recall that the measure of interest is the stress triaxiality or Lode angle and that the input involves the uncertain material parameters. Thus, Sobol' indices can reveal which of the material parameters characterizing the material behavior is the most influential regarding the measure of interest. Such information is most valuable as, for example, one may decide to collect additional information on that material parameter to either reduce its uncertainty or take appropriate measures that ameliorate its effect on stress triaxiality and ultimately, damage on metal forming processes. This similarly applies to other stress-based measures established to predict damage related effects, evolution and performance, such as the related Lode angle.

The practical calculation of Sobol' indices is most demanding from a numerical viewpoint (see, e.g. Saltelli et al. (2008) and Patelli et al. (2010)). Indeed, such calculation involves repeated evaluations of the measure of interest for different combinations of the input material parameters, possibly in the order of tens of thousands. Considering that the solution of a single nonlinear finite element simulation may demand minutes, hours or even days of CPU time (depending on the complexity of the underlying model), the direct calculation of Sobol' indices is usually not feasible from a computational viewpoint. Hence, specialized numerical approaches are required for their calculation in practical problems (see, e.g. Sudret (2008)).

Taking into account the challenges described above, the objective of this work is to implement a framework for performing computationally efficient variance-based global sensitivity analysis of the stress triaxiality and Lode angle of a mechanical component. Sensitivity is considered with respect to the material parameters characterizing an elasto-plastic stress–strain material behavior. The focus is on conducting a sensitivity analysis which is efficient from a numerical viewpoint and that demands a limited number of evaluations of the associated nonlinear finite element model. In particular, this work implements a framework introduced in Song et al. (2022) to yield the calculation of Sobol' indices feasible. The framework involves constructing a Gaussian process regression (Rasmussen and Williams, 2006), which replaces (or surrogates) the nonlinear finite element model and which can be evaluated at negligible numerical costs. This Gaussian process is trained with a limited number of realizations of the finite element model (usually in the order of a few tens). In a post-processing step, the Gaussian process is employed within a Bayesian probabilistic integration framework (Briol et al., 2019), that allows calculating the sought Sobol' indices. Furthermore, Bayesian probabilistic integration allows quantifying the error in the estimates that it produces. These error estimates are most useful for improving the Gaussian process regression on-the-fly through active learning (Jones et al., 1998), thus allowing to enhance the estimates of the Sobol' indices with additional evaluations of the finite element model.

The rest of this paper is organized as follows: Section 2 describes the class of problems considered in this contribution from a purely deterministic viewpoint. That is, essentials of the background on the assessment of stress triaxiality and Lode angle for materials with fixed material parameters and exhibiting elasto-plastic response with proportional hardening are (briefly) summarized. The particular model also serves for the subsequent finite element analysis. Section 3 describes the framework for uncertainty quantification and global sensitivity analysis of stress triaxiality and Lode angle with respect to material properties. Concepts such as Sobol' indices, Gaussian processes and Bayesian probabilistic integration are explained in depth. The framework developed in the aforementioned two sections is put into practice in Section 4, where sensitivity analysis of a tensile test specimen is carried out. This work closes with a summary and outlook in Section 5.

2. Elasto-plasticity framework

This section briefly introduces essential kinematic relations, mentions the underling balance equation (in strong form) and provides basic background on the finite deformation elasto-plasticity framework applied in this work. Further details on the general theory and implementation are addressed in Simo (1998), or e.g. Sprave and Menzel (2020), even though the present paper does not focus on ductile damage modeling, and references cited therein.

2.1. Essential kinematics

A finite deformation setting shall be considered, with referential placements in the reference configuration denoted by $\boldsymbol{X} \in \mathcal{B}_0$, whereas spatial placements in the spatial configuration are represented by $\boldsymbol{x} \in \mathcal{B}_t$. The motion is introduced as a nonlinear mapping and, together with the related so-called deformation gradient, denoted as

$$\boldsymbol{x} = \boldsymbol{\varphi}(\boldsymbol{X}, t) \quad \text{and} \quad \boldsymbol{F} = \nabla_{\boldsymbol{X}} \boldsymbol{\varphi} \,, \tag{1}$$

wherein t represents time and $J = \det(\boldsymbol{F}) > 0$.

A multiplicative decomposition of the deformation gradient into an elastic (e) and plastic (p) contribution is assumed as this work proceeds,

i.e. $\boldsymbol{F} = \boldsymbol{F}_\mathrm{e} \cdot \boldsymbol{F}_\mathrm{p}$ with $J_\mathrm{e} = \det(\boldsymbol{F}_\mathrm{e}) > 0$. These deformation quantities allow introduction of representative strain measure such as spatial elastic logarithmic strains of the form

$$\boldsymbol{\varepsilon}_\mathrm{e} = \tfrac{1}{2}\ln(\boldsymbol{F}_\mathrm{e}\cdot\boldsymbol{F}_\mathrm{e}^\mathrm{t}) = \tfrac{1}{2}\ln(\boldsymbol{b}_\mathrm{e}) = \boldsymbol{\varepsilon}_\mathrm{e}^\mathrm{vol} + \boldsymbol{\varepsilon}_\mathrm{e}^\mathrm{iso}\,, \tag{2}$$

wherein $\bullet^\mathrm{t}$ denotes transposition and $\boldsymbol{\varepsilon}_\mathrm{e}^\mathrm{vol} = \frac{1}{3}\operatorname{tr}(\boldsymbol{\varepsilon}_\mathrm{e})\,\boldsymbol{I}$ with $\boldsymbol{I}$ the second-order identity tensor.

2.2. Finite isotropic elasto-plasticity

The Helmholtz energy is considered for an isothermal setting and assumed to decompose additively into an elastic volumetric, an elastic isochoric and a proportional hardening related contribution of the form

$$\Psi(\boldsymbol{b}_\mathrm{e},\alpha) = \tfrac{1}{2}K\operatorname{tr}^2(\boldsymbol{\varepsilon}_\mathrm{e}) + G\operatorname{tr}(\boldsymbol{\varepsilon}_\mathrm{e}^\mathrm{iso}\cdot\boldsymbol{\varepsilon}_\mathrm{e}^\mathrm{iso}) + \frac{h}{n_\mathrm{p}+1}\,\alpha^{n_\mathrm{p}+1}\,, \tag{3}$$

wherein α is a proportional hardening related internal variable and K, G, h, n_p are material parameters.

Based on this (isotropic) specification, the (mechanical) dissipation contribution results in

$$\mathcal{D} = \boldsymbol{m}^\mathrm{t} : \boldsymbol{l} - \dot{\Psi} = \boldsymbol{m}^\mathrm{t} : \boldsymbol{l}_\mathrm{p} + \beta\,\dot{\alpha} \geq 0\,, \tag{4}$$

wherein $\dot{\bullet}$ denotes the material time derivative, $\boldsymbol{l} = \nabla_{\boldsymbol{x}}\dot{\boldsymbol{\varphi}} = \boldsymbol{l}_\mathrm{e} + \boldsymbol{l}_\mathrm{p}$ with $\boldsymbol{l}_\mathrm{p} = \boldsymbol{F}_\mathrm{e}\cdot\dot{\boldsymbol{F}}_\mathrm{p}\cdot\boldsymbol{F}^{-1}$, together with

$$\boldsymbol{m}^\mathrm{t} = 2\,\frac{\partial\Psi}{\partial\boldsymbol{b}_\mathrm{e}}\cdot\boldsymbol{b}_\mathrm{e} \quad\text{and}\quad \beta = -\frac{\partial\Psi}{\partial\alpha} = -\,h\,\alpha^{n_\mathrm{p}}\,. \tag{5}$$

Stresses $\boldsymbol{m}$ can be interpreted as spatial Mandel-type stresses, are further specified in e.g. Sprave and Menzel (2020), and relate to the Kirchhoff stresses via the spatial contra-variant metric tensor, i.e. $\boldsymbol{\tau} = \boldsymbol{g}^{-1}\cdot\boldsymbol{m}^\mathrm{t} = \boldsymbol{\tau}^\mathrm{t}$.

In this work rate-independent von Mises plasticity is considered in combination with nonlinear proportional hardening. The related yield function reads

$$\Phi(\boldsymbol{m}^\mathrm{t},\beta) = \|\boldsymbol{m}^{\mathrm{t}\,\mathrm{dev}}\| - \sqrt{\tfrac{2}{3}}\,[\,\sigma_{y0} - \beta\,]\,, \tag{6}$$

with $\boldsymbol{m}^{\mathrm{t}\,\mathrm{dev}} = \boldsymbol{m}^\mathrm{t} - \frac{1}{3}\operatorname{tr}(\boldsymbol{m}^\mathrm{t})\,\boldsymbol{I}$ and $\|\bullet\| = \sqrt{\bullet:\bullet}$. This yields the set of material parameters considered, here represented in vectorial form, as $\boldsymbol{\theta} = [K\ G\ \sigma_{y0}\ h\ n_\mathrm{p}]$.

Moreover, associative plastic flow is considered so that

$$\boldsymbol{l}_\mathrm{p} = \lambda\,\frac{\partial\Phi}{\partial\boldsymbol{m}^\mathrm{t}} = \lambda\,\frac{\boldsymbol{m}^{\mathrm{t}\,\mathrm{dev}}}{\|\boldsymbol{m}^{\mathrm{t}\,\mathrm{dev}}\|}\,, \tag{7}$$

$$\dot{\alpha} = \lambda\,\frac{\partial\Phi}{\partial\beta} = \lambda\,\sqrt{\tfrac{2}{3}}\,, \tag{8}$$

together with the Karush-Kuhn–Tucker conditions $\Phi \leq 0$, $\lambda \geq 0$, and $\lambda\,\Phi = 0$. While Euler backward integration is applied to the proportional hardening variable, i.e. $\alpha_{n+1} = \alpha_n + \sqrt{2/3}\,\Delta\lambda$ for $\Delta\lambda = \Delta t\,\lambda$ and time increment $\Delta t = t_{n+1} - t_n$, plastic incompressibility preserving exponential integration is applied to $\boldsymbol{l}_\mathrm{p}$, respectively $\boldsymbol{F}_\mathrm{p}$; see, e.g., Simo (1998) and Sprave and Menzel (2020) for further details.

2.3. Balance of linear momentum

An isothermal setting shall be considered in this work. In consequence, the only balance equation to be solved is the balance of linear momentum, with balance of angular momentum intrinsically satisfied by the symmetry of Kirchhoff stresses $\boldsymbol{\tau}$, respectively symmetry of Cauchy stresses $\boldsymbol{\sigma} = \boldsymbol{\tau}/J = \boldsymbol{\sigma}^\mathrm{t} = \sigma_i\,\boldsymbol{n}_i\otimes\boldsymbol{n}_i$, whereby σ_i denote the principal stresses with related principal vectors $\boldsymbol{n}_i$. Neglecting acceleration contributions and volume forces, balance of linear momentum in local form and spatial representation reduces to

$$\nabla_{\boldsymbol{x}}\cdot\boldsymbol{\sigma} = \boldsymbol{0} \text{ in } \mathcal{B}_t \quad\text{and}\quad \boldsymbol{\sigma}\cdot\boldsymbol{n} = \bar{\boldsymbol{t}} \text{ on } \partial\mathcal{B}_t^t\,, \tag{9}$$

wherein $\boldsymbol{n}$ denotes the normal surface unit vector and $\bar{\boldsymbol{t}}$ the prescribed traction vector on the Neumann boundary $\partial\mathcal{B}_t^t$. The global weak form representation of Eq. (9) is the basis of the (implicit) finite element formulation considered as this work proceeds.

Different stress-based measures represent local loading states most relevant for reliable prediction purpose of, e.g., damage states and failure initiation processes. In this work, such measures are referred to the Cauchy stresses $\boldsymbol{\sigma}$. Basic measures are the hydrostatic stress state σ_m, the von Mises equivalent stress σ_e, and stress triaxiality η, i.e.

$$\sigma_m = \tfrac{1}{3}\operatorname{tr}(\boldsymbol{\sigma})\,, \quad \sigma_e = \sqrt{\tfrac{3}{2}}\,\|\boldsymbol{\sigma}^\mathrm{dev}\|\,, \quad \eta = \frac{\sigma_m}{\sigma_e}\,, \tag{10}$$

see, e.g., Davis and Connelly (1959) in view of application of stress triaxiality in metal plasticity. Moreover, the Lode angle ϑ, as introduced in Lode (1926), represents properties of the stress state, namely the orientation of the stress state within its octahedral plane in principal stress space. To be specific, the Lode angle ϑ can be generated based on the stress mode (triaxiality) factor ζ via

$$\zeta = \frac{\sqrt{27}}{2}\,\frac{J_3}{J_2^{3/2}} = \frac{27}{2}\,\frac{J_3}{\sigma_e^3} \quad\text{and}\quad \vartheta = \tfrac{1}{3}\arccos(\zeta)\,, \tag{11}$$

with the (deviatoric) Cauchy stress invariants $J_2 = \frac{1}{2}\operatorname{tr}(\boldsymbol{\sigma}^\mathrm{dev}\cdot\boldsymbol{\sigma}^\mathrm{dev}) = \frac{1}{2}\,\|\boldsymbol{\sigma}^\mathrm{dev}\|^2 = \frac{1}{3}\,\sigma_e^2$ and $J_3 = \det(\boldsymbol{\sigma}^\mathrm{dev})$.

3. Uncertainty quantification and sensitivity analysis

The preceding section has discussed the calculation of stress triaxiality and Lode angle for a mechanical component. In this section, the aim is to study the sensitivity of stress triaxiality and Lode angle with respect to the material parameters. For that purpose, Section 3.1 explains how the finite element analysis is abstracted as a black-box function. Then, the characterization of uncertainty on material parameters is addressed in Section 3.2. Probabilistic descriptors for characterizing uncertainty and performing sensitivity analysis of the measures of interest (either stress triaxiality or Lode angle) are described in Sections 3.3 and 3.4. The numerical strategies for calculating these descriptors are discussed in detail in Sections 3.5 and 3.6.

3.1. Abstraction of the finite element analysis as a black-box

The measures of interest (stress triaxiality and Lode angle) are calculated by means of a nonlinear finite element model. The different material parameters associated with this model – that is bulk modulus K, shear modulus G, yield stress σ_{y0}, hardening modulus h, and hardening exponent n_p – are collected in vector $\boldsymbol{\theta}$, cf. Section 2.2. In addition, recall that the stress triaxiality η as well as the Lode angle ϑ are scalar quantities with the respective values dependent on position $\boldsymbol{x} \in \mathcal{B}_t$, respectively $\boldsymbol{X} \in \mathcal{B}_0$, as well as on the particular values of the material parameters included in $\boldsymbol{\theta}$. In order to perform sensitivity analysis, stress triaxiality and Lode parameter are synthesized each in a single scalar quantity by considering the respective maximum value of its field distribution. The subsequent analysis shall emphasis one such maximum value and the framework similarly applied to both, stress triaxiality η and Lode angle ϑ. In this context, let such maximum value be denoted as y, introduced as

$$y = \max_{\{\boldsymbol{X},t\}\in\mathcal{B}_0\times\mathbb{R}} (\eta(\boldsymbol{X},t,\boldsymbol{\theta}))\,, \tag{12}$$

where $\max(\bullet)$ is a function that returns the maximum value of the argument. This last equation can be rewritten in compact form as

$$y = g(\boldsymbol{\theta}), \tag{13}$$

where $g(\bullet)$ denotes a function that involves taking the maximum value of the measure of interest from a nonlinear finite element analysis of the mechanical component under consideration for a given set of values of the material parameter vector and along prescribed boundary conditions, respectively loading history. Clearly, Eq. (13) provides a compact, abstract representation of the finite element analysis as a black-box function.

3.2. Uncertainty characterization of material parameters

It is assumed that the material parameters $\boldsymbol{\theta}$ governing the stress–strain relations are uncertain. Such assumption is often met in reality: due to variability in raw materials and manufacturing process of steel, it may be challenging to identify these parameters in a crisp manner. A possible means to quantify the uncertainty associated with these parameters is resorting to probability theory, see e.g. Elnashai and Chryssanthopoulos (1991). Under such framework, it is considered that $\boldsymbol{\theta}$ is actually a realization of a random variable vector $\boldsymbol{\Theta}$. The components of $\boldsymbol{\Theta}$ are considered as independent and therefore, the joint probability density function becomes $f_{\boldsymbol{\Theta}}(\boldsymbol{\theta}) = \prod_{i=1}^{n_\theta} f_{\Theta_i}(\theta_i)$, where θ_i denotes the ith component of $\boldsymbol{\theta}$; $f_{\Theta_i}(\theta_i)$ is the probability density function associated with Θ_i, which is the ith component of the random variable vector $\boldsymbol{\Theta}$; and n_θ the number of material parameters ($n_\theta = 5$ in this case). It is assumed that $f_{\Theta_i}(\theta_i)$, $i = 1, \dots, n_\theta$ is prescribed for $i = 1, \dots, n_\theta$. Nonetheless, in a more general situation, it is possible to infer $f_{\Theta_i}(\theta_i)$, for $i = 1, \dots, n_\theta$, based on prior knowledge and actual measurements through Bayesian updating; see e.g. Sivia (1996), or resort to more general models for the description of the uncertainty (Faes et al., 2021).

As the uncertainty associated with material parameters $\boldsymbol{\theta}$ is modeled through random variables and considering the relation established in Eq. (13), the maximum value y becomes uncertain as well. That is, y is actually a realization of a random variable Y. To quantify the uncertainty associated with the maximum value y, one can resort to probabilistic descriptors, such as mean and variance or variance-based global sensitivity analysis, as discussed in Sections 3.3 and 3.4, respectively.

3.3. Mean and variance

A simple means for quantifying the uncertainty associated with the maximum value y is calculating its second-order statistics, namely expected value $\mathbb{E}_{\boldsymbol{\Theta}}(y)$ and variance $\mathbb{V}_{\boldsymbol{\Theta}}(y)$, which are defined as (see, e.g., Fishman (1996))

$$\mathbb{E}_{\boldsymbol{\Theta}}(y) = \int_{\boldsymbol{\theta}\in\Omega_{\boldsymbol{\theta}}} g(\boldsymbol{\theta}) f_{\boldsymbol{\Theta}}(\boldsymbol{\theta})\, \mathrm{d}\boldsymbol{\theta}\,, \tag{14}$$

$$\mathbb{V}_{\boldsymbol{\Theta}}(y) = \int_{\boldsymbol{\theta}\in\Omega_{\boldsymbol{\theta}}} \left(g(\boldsymbol{\theta}) - \mathbb{E}_{\boldsymbol{\Theta}}(y)\right)^2 f_{\boldsymbol{\Theta}}(\boldsymbol{\theta})\, \mathrm{d}\boldsymbol{\theta}\,, \tag{15}$$

where $\Omega_{\boldsymbol{\theta}}$ denotes the support of $\boldsymbol{\theta}$.

Expected value and variance are most useful for providing a rough idea on the uncertainty associated with stress triaxiality, respectively Lode angle. In fact, variance measures the *level of dispersion* and can provide an intuitive means for assessing the ranges in which these stress quantities may vary. Nonetheless, second-order statistics are generally regarded as a first step in an uncertainty quantification analysis. Therefore, more advanced probabilistic descriptors must be considered, such as variance-based global sensitivity indices, as discussed in the next section.

3.4. Variance-based global sensitivity indices

Variance-based sensitivity analysis aims at apportioning the variance of the response of interest (in this case stress triaxiality and Lode angle) with respect to the parameters that affect that response (in this case the material parameters). The result of the sensitivity analysis is expressed in terms of the so-called Sobol' indices (Sobol', 1993). The *first-order* (or main) Sobol' sensitivity indices S_i are defined as (see, e.g. Saltelli et al. (2008))

$$S_i = \frac{\mathbb{V}_{\Theta_i}\left(\mathbb{E}_{\boldsymbol{\Theta}_{-i}}\left(y|\theta_i\right)\right)}{\mathbb{V}_{\boldsymbol{\Theta}}(y)}, \quad i = 1, \dots, n_\theta \tag{16}$$

wherein $\mathbb{V}_{\Theta_i}(\cdot)$ denotes that variance is calculated only with respect to Θ_i. Moreover, $\boldsymbol{\Theta}_{-i}$ is the vector of all random variables except for Θ_i; $\mathbb{E}_{\boldsymbol{\Theta}_{-i}}(\cdot)$ denotes expectation with respect to $\boldsymbol{\Theta}_{-i}$; and $y|\theta_i$ denotes that the maximum value y is calculated considering a fixed value θ_i for the ith material parameter. The first-order Sobol' index S_i as shown in Eq. (16) can be interpreted as follows.

- Its numerator represents the variance with respect to ith material parameter (associated with Θ_i) once the effects of the remaining material parameters (associated with $\boldsymbol{\Theta}_{-i}$) have been averaged by means of the conditional expectation.
- Its denominator represents the total variance.

Thus, the first-order Sobol' index is a dimensionless quantity that expresses the fraction of the variance associated with the maximum value y that can be attributed to the uncertainty of the ith material parameter. For those cases where the ith material parameter has a high impact on y with respect to the remaining material parameters, it is expected that the aforementioned numerator will be close to the denominator and thus the Sobol' index will be close to 1 while the opposite holds true. It is noted that first-order Sobol' indices are always bounded between zero and one, that is $0 \le S_i \le 1$ for $i = 1, \dots, n_\theta$. Moreover, the summation of all first-order Sobol' indices is always equal or smaller than one, that is $\sum_{i=1}^{n_\theta} S_i \le 1$. Whenever the summation of the first-order Sobol' indices is close to 1, one is in presence of a so-called additive model, meaning that there are no significant interaction effects between the different material parameters and hence, the variability of the output response (in this case stress triaxiality and Lode angle) is mainly explained as the superposition of the individual effects of each input (in this case material parameters).

In addition to the first-order sensitivity indices, there are also the so-called total Sobol' sensitivity indices $S_{T,i}$, which are defined as (see, e.g. Saltelli et al. (2008))

$$S_{T,i} = \frac{\mathbb{V}_{\boldsymbol{\Theta}}(y) - \mathbb{V}_{\boldsymbol{\Theta}_{-i}}\left(\mathbb{E}_{\Theta_i}\left(y|\boldsymbol{\theta}_{-i}\right)\right)}{\mathbb{V}_{\boldsymbol{\Theta}}(y)}, \quad i = 1, \dots, n_\theta\,. \tag{17}$$

From the above equation, note that $\mathbb{V}_{\boldsymbol{\Theta}_{-i}}\left(\mathbb{E}_{\Theta_i}\left(y|\boldsymbol{\theta}_{-i}\right)\right)$ represents the variance that can be attributed to all material parameters except for the ith one (that is, the variance associated with $\boldsymbol{\Theta}_{-i}$) once the effect of the ith material parameter has been averaged by means of the conditional expectation. Thus, the subtraction between $\mathbb{V}_{\boldsymbol{\Theta}}(y)$ and $\mathbb{V}_{\boldsymbol{\Theta}_{-i}}\left(\mathbb{E}_{\Theta_i}\left(y|\boldsymbol{\theta}_{-i}\right)\right)$ in the numerator of Eq. (17) represents the variance that can be attributed to uncertainty in the ith material parameter and its interaction with other material parameters. The total sensitivity indices are always bounded between zero and one, just like the first-order sensitivity indices, that is $0 \le S_{T,i} \le 1$ for $i = 1, \dots, n_\theta$. Furthermore, the total sensitivity index associated with the ith variable will be always equal or larger than its first-order counterpart, that is $S_{T,i} \ge S_i$ for $i = 1, \dots, n_\theta$. A significant difference between $S_{T,i}$ and S_i may reveal a strong interaction of the ith material parameter and the other material parameters on the variance of the maximum stress triaxiality or Lode angle, respectively (Patelli et al., 2010).

3.5. Calculation of probabilistic descriptors

The probabilistic descriptors presented in Sections 3.3 and 3.4 are calculated by means of surrogate modeling, see e.g. Sudret (2008). In this way, it is possible to avoid repeated and numerically costly nonlinear finite element analyses. Section 3.5.1 describes Gaussian process regression (GPR), which is the type of surrogate model considered in this work. The calculation of the probabilistic descriptors is carried out by performing Bayesian probabilistic integration over the GPR surrogate model, as considered in Section 3.5.2. In addition, the accuracy of the calculated probabilistic descriptors can be improved by refining the GPR through active learning, as discussed in detail in Section 3.5.3.

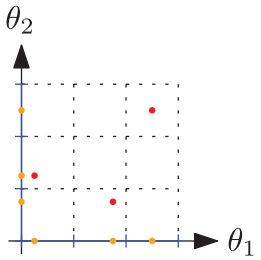

Fig. 1. Schematic representation of Latin hypercube sampling. (For interpretation of the references to color in this figure legend, the reader is referred to the web version of this article.)

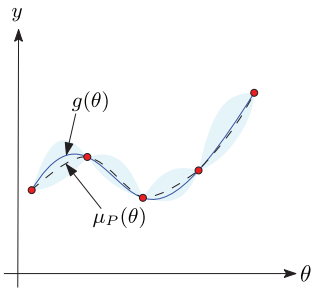

Fig. 2. Schematic representation of Gaussian process regression. (For interpretation of the references to color in this figure legend, the reader is referred to the web version of this article.)

3.5.1. Gaussian process regression

A surrogate is a mathematical model which is inexpensive to calculate and that approximates a function whose evaluation is numerically involved. There are several types of surrogate models available, such as polynomial response surface, polynomial chaos and artificial neural networks, to name a few (see, e.g., Faravelli (1989), Hurtado and Alvarez (2001) and Sudret (2008)). One of the most popular surrogate models is Gaussian process regression (GPR), as it provides both an estimate of the function being surrogated as well as a measure on the level of confidence of that estimate (Rasmussen and Williams, 2006). Therefore, GPR is considered in this work.

The first step for constructing a GPR is choosing its prior, which means defining its parametric form in terms of a mean $\mu_I(\boldsymbol{\theta})$ and covariance function $\kappa_I(\boldsymbol{\theta}, \boldsymbol{\theta}')$. Note that the mean $\mu_I(\boldsymbol{\theta})$ expresses expected value of y at $\boldsymbol{\theta}$ while the covariance $\kappa_I(\boldsymbol{\theta}, \boldsymbol{\theta}')$ represents the joint variability between y and y' for two different realizations $\boldsymbol{\theta}$ and $\boldsymbol{\theta}'$ of the material parameters. Without loss of generality and for simplicity, the mean function can be chosen as a real constant μ_0 while the covariance can be chosen as a squared exponential function:

$$\kappa_I(\boldsymbol{\theta}, \boldsymbol{\theta}') = \sigma_0^2 \exp\left(-\frac{1}{2}\sum_{i=1}^{n_\theta}\left[\frac{\theta_i - \theta_i'}{L_i}\right]^2\right) \tag{18}$$

where σ_0^2 is the variance of the prior GPR and L_i, for $i = 1, \ldots, n_\theta$, are scale length parameters associated with each of the material parameters. It is noted that the GPR previously described involves a total of $(n_\theta + 2)$ hyperparameters $\left[\mu_0 \ \sigma_0^2 \ L_1 \ \ldots \ L_{n_\theta}\right]$ which must be identified. For that purpose, it is necessary to generate a set of *training* data points $(\boldsymbol{y}_d, \boldsymbol{\Theta}_d)$, where $\boldsymbol{y}_d$ is a vector of dimension n_d while $\boldsymbol{\Theta}_d$ is a matrix of dimension $n_d \times n_\theta$. The jth row of matrix $\boldsymbol{\Theta}_d$ contains a realization $\theta^{(j)}$ of the material parameters while the jth entry of vector $\boldsymbol{y}_d$ contains the maximum value y associated with that realization, that is, $y_D^{(j)} = g\left(\theta^{(j)}\right)$. The latter step implies that a total of n_d nonlinear finite element analyses must be carried out. The set of realizations $\boldsymbol{\Theta}_d$ for training the GPR is usually generated by means of a design-of-experiments scheme such as Latin hypercube sampling (McKay et al., 1979). This sampling scheme is illustrated in Fig. 1 and it involves two main concepts. First, the space of feasible values for each random variable θ_i is divided into strata of equal probability (represented with blue color in Fig. 1) and then, a random sample is drawn into each strata (represented with orange dots in Fig. 1). Second, the samples associated with the different random variables are paired at random. These randomly paired samples are shown with red dots in Fig. 1. In practical applications, it has been observed that Latin hypercube sample offers an excellent balance between space coverage and robustness with respect to the number of involved random variables n_θ.

Once that the training data set has been generated, the hyperparameters $\left[\mu_0 \ \sigma_0^2 \ L_1 \ \ldots \ L_{n_\theta}\right]$ of the GPR are inferred by maximum likelihood, which is a well-established statistical procedure for identifying parameters of a probability model (see, e.g., Rasmussen and Williams (2006)). After identifying the hyperparameters of the GPR model, it is possible to predict maximum value y for an arbitrary realization of the material parameters $\boldsymbol{\theta}^*$. For that purpose, one considers the hyperparameters identified previously in combination with the training data set $(\boldsymbol{y}_d, \boldsymbol{\Theta}_d)$, which leads to the posterior mean $\mu_P(\boldsymbol{\theta})$ and posterior covariance $\kappa_P(\boldsymbol{\theta}, \boldsymbol{\theta}')$. In this sense, the term *posterior* indicates that all available information is reflected into the mean and covariance. To further discuss this point, consider Fig. 2, that illustrates a Gaussian process regression which, for simplicity, depends on a single material parameter θ. The training set consists of $n_d = 5$ points, which are denoted with red dots in the figure. This means that five values of the material parameter $\theta^{(j)}$, for $j = 1, \ldots, 5$, were generated using a design-of-experiments scheme and that for each of those values, the maximum value $y_d^{(j)} = g\left(\theta^{(j)}\right)$, for $j = 1, \ldots, 5$, was calculated by means of nonlinear finite element analysis. After identifying the hyperparameters of the GPR and taking into account the training data, it is possible to deduce the posterior mean value $\mu_P(\theta)$, which is the dashed black line in the figure. It is observed that this dashed line passes over each of the training data points and that it closely mimics the *true* curve $g(\theta)$. Furthermore, the posterior covariance $\kappa_P(\theta, \theta')$ quantifies the amount of uncertainty regarding the prediction of the Gaussian process regression and is shown in the figure as a confidence interval around the mean $\mu_P(\theta)$ by means of the cyan shaded area. It is noted that at the training data points the confidence interval collapses, as in those points there is actually no uncertainty: the value of y is known *exactly* as it was evaluated using nonlinear finite element analyses.

3.5.2. Bayesian probabilistic integration

The probabilistic descriptors described in Sections 3.3 and 3.4 must be computed by solving multidimensional integrals that comprise the maximum value of interest as a function of the material parameters. To avoid repeated nonlinear finite element analyses, the maximum value is approximated by means of a GPR surrogate model, as described previously. However, it should be recalled that for a given value of the material parameters, the GPR model provides both an estimate of the maximum value of interest as well as the level of confidence on that estimate. This is a salient feature from a practical viewpoint for calculating the respective probabilistic descriptor. For example, if the aim is calculating the expected value as shown in Eq. (14) and the GPR model is considered, it is possible to produce a mean estimate (that is, the *mean of the expectation*) as well as the variance of that estimate (that is, the *variance of the expectation*). The latter variance is most important, as it expresses the degree of uncertainty in the estimation of a probabilistic descriptor due to the surrogate model.

The task of producing estimates of the probabilistic descriptors as well as a measure of their uncertainty based on the GPR surrogate is carried out by means of Bayesian probabilistic integration; see, e.g., Briol et al. (2019). In fact, in this work the Bayesian probabilistic integration approach developed in Song et al. (2022) is implemented, in which

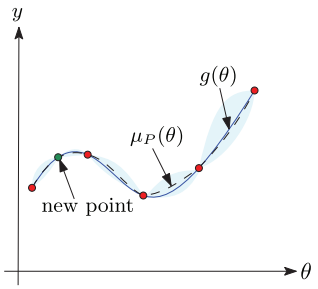

Fig. 3. Schematic representation of Gaussian process regression with additional training data point. (For interpretation of the references to color in this figure legend, the reader is referred to the web version of this article.)

- The mean and variance of the expectation (see Eq. (14)) are calculated by means of closed-form solutions.
- The mean and variance of the variance (see Eq. (15)) as well as the variances associated with the first and total order Sobol' indices (see Eqs. (16) and (17)) can be calculated through analytical expressions that are integrated numerically (that is, partially closed form).

The specific expressions associated with Bayesian probabilistic integration of the mean, variance, first-order and total order Sobol' indices are not reproduced in here due to their length. Detailed derivations, as well as specific expressions for computing these probabilistic descriptors, can be found in Song et al. (2022).

3.5.3. Active learning

Bayesian probabilistic integration provides the mean estimate of a probabilistic descriptor as well its variance. This variance provides important information for deciding whether the current GPR model provides sufficiently accurate estimates of the sought probabilistic descriptors. If the variance is too high, one may decide to improve the quality of the estimate by including an additional training data point and updating the GPR model. Fig. 3 illustrates this idea. In fact, Fig. 3 is identical to Fig. 2, except that an additional training point marked with green color is introduced. As noted from the figure, the mean of the GPR $\mu_P(\theta)$ reproduces almost exactly the reference curve $g(\theta)$ at the left hand side of the plot while the confidence interval collapses almost to zero, revealing a high degree of confidence regarding the prediction provided by the GPR model in that location. This is due to the inclusion of the new data point in green color.

The process of selecting a new training data point for improving the GPR surrogate model can be interpreted as a refinement or enrichment procedure. In practice, it has been observed that such data point can be selected by maximizing a so-called *learning* function that involves the variance associated with the probabilistic descriptor in Eq. (15), that is, the *variance of the variance*, see Song et al. (2022). This learning function balances the expected improvement in the variance estimator versus the likelihood of observing a particular combination of material parameters $\boldsymbol{\theta}$. More importantly, this learning function involves evaluating the GPR model only. Hence, nonlinear finite element analysis is carried out once the new point for enlarging the training data set has been identified. Specific details about the learning function considered in this work can be found in Song et al. (2022).

The procedure for improving the accuracy of the probabilistic descriptors described above can be regarded as *active learning*. Indeed, starting from an initial data set generated with Latin hypercube sampling for training the GPR surrogate model, one assesses the quality of the estimated probabilistic descriptors and decides to improve their quality based on the variance associated with those descriptors. Then, one identifies a new training data point and performs an additional nonlinear analysis, which allows to enlarge the training data set and to improve both the quality of the GPR and the accuracy of the estimated probabilistic descriptors.

Table 1
Reference material parameter set (ref.) identified for DP800 steel, taken from Sprave and Menzel (2020), and upper (u.b.) and lower bound (l.b.) used for uncertainty quantification.

	K [GPa]	G [GPa]	σ_{y0} [MPa]	h [MPa]	n_p [−]
u.b	124.92	89.82	273.45	1876.20	0.2389
ref.	118.97	85.54	248.59	1705.64	0.2654
l.b.	113.02	81.26	223.73	1535.08	0.2920

3.6. Outline of procedure for uncertainty quantification

From an algorithmic viewpoint, the framework of uncertainty quantification in elasto-plasticity presented in Sections 2 and 3 can be summarized in the following steps.

1. Set up a nonlinear finite element model of the mechanical component of interest that allows calculating maximum stress triaxiality and maximum Lode parameter.
2. Characterize the uncertainty regarding material parameters using appropriate probability distributions.
3. Generate a set of training data points involving realizations of the material parameters and compute their respective maximum stress triaxiality and maximum Lode parameter by means of the nonlinear finite element model established in step 1.
4. Train the GPR surrogate model and calculate probabilistic descriptors using Bayesian probabilistic integration.
5. Check the variance of the estimated probabilistic descriptors. If the variance is too high, identify an additional point in the training data set through active learning, perform nonlinear finite element analysis and return to step 4. Otherwise, retain the current probabilistic descriptors and finish the procedure.

All of these algorithmic steps have been implemented within in-house software. Uncertainty quantification (involving sampling, Gaussian process regression and Bayesian probabilistic integration) has been implemented in Matlab. Routines for analysis of elasto-plasticity within the nonlinear finite element method have been implemented using C++.

4. Example

In this section, the effect of uncertainty of material parameters on damage initiation indicators of stress triaxiality and Lode angle is quantified for an exemplary boundary value problem of a plastically deforming mechanical component. For this purpose, the computationally efficient variance-based global sensitivity analysis strategy proposed in Section 3 is applied to a finite element model of a tensile test specimen. Basic characteristics and properties of the underlying material model are analyzed in Appendix, where states under uniaxial tension are considered.

In this regard, a nonlinear finite element model for the boundary value problem considered is established to identify maximum stress triaxiality and Lode angle values on the Gauss point level. This is achieved by evaluating the finite elasto-plasticity constitutive model outlined in Section 2.2 for a given set of material parameters. The uncertainty associated with the material parameters characterizing elasto-plasticity is described via the axioms of probability theory. Uniform distributions with lower and upper bounds, as described in Table 1, are assumed. The respective GPR surrogate model is trained based on stress triaxiality, respectively Lode angle, obtained on the Gauss point level as maximum values over the entire loading history. Finite element analyses are conducted for an initial batch of training data points, i.e. sets of material parameters. The initial training data set is generated by Latin hypercube sampling through a design-of-experiments scheme and is applied to both GPR surrogate models of maximum stress triaxiality and Lode angle. A subsequent active learning strategy further enhances each GPR surrogate model through finite element simulation evaluations

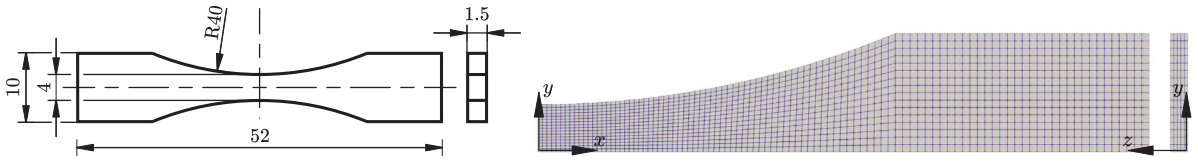

(a) Tensile test specimen geometry and dimensions. (b) Spatial discretization of the tensile test specimen.

Fig. 4. Tensile test specimen geometry and dimensions in millimeters taken from Sprave and Menzel (2020). A spatial discretization of $n_{el} = 8000$ eight-noded trilinear hexahedral F-bar elements with full integration is motivated by a mesh convergence study at a maximum tensile displacement of $u_x = 0.65$ mm on the basis of reaction force history, maximum stress triaxiality and Lode angle.

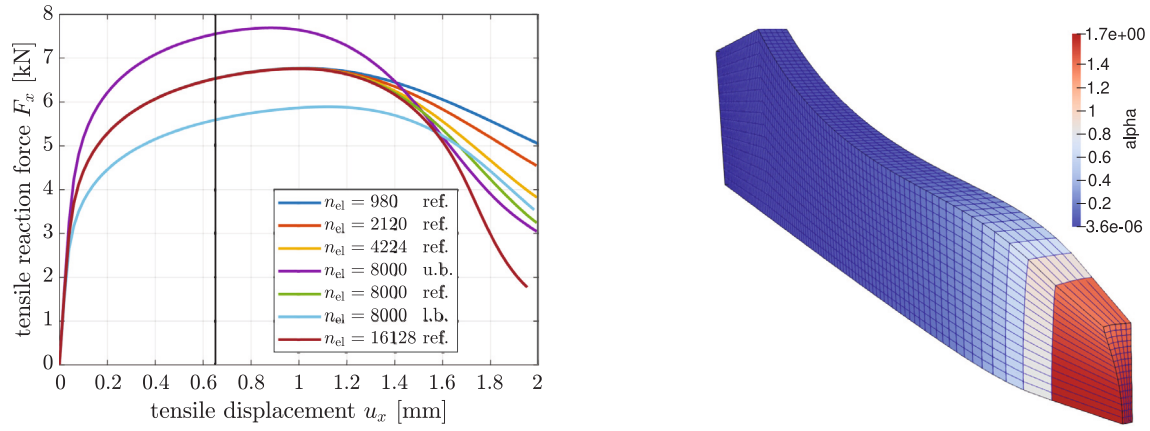

(a) Force-displacement curves for different discretizations n_{el}. (b) Localization of the proportional hardening variable α.

Fig. 5. Mesh convergence study for full loading of $u_x = 2$ mm shows mesh-dependent results due to severe necking. Localization of the proportional hardening variable α in one single element row for $n_{el} = 8000$ observed for the reference material parameter set at a maximum tensile displacement of $u_x = 2$ mm.

at additional training data points generated by maximizing the so-called learning function. Active learning is continued until convergence in the maximum coefficient is achieved for the variances involved in the analysis; that is, total or partial variances, as appearing in Eqs. (15), (16) and (17). In this context, note that the coefficient of variation represents the square root of the variance of an estimator divided by the expected value of that estimator. The converged Sobol' sensitivity indices for both damage initiation indicators resulting from Bayesian probabilistic integration over the respective GPR surrogate model are analyzed regarding the most influential material parameters and interaction effects between the material parameters. Thus, uncertainty on maximum stress triaxiality and Lode angle is identified and characterized.

4.1. Boundary value problem

The underlying material model is applied to the finite element setting for solving a boundary value problem of a tensile test specimen. This enables a first investigation of the effects of material parameters on the damage initiation indicators of stress triaxiality and Lode angle. To this end, a nonlinear finite element model is set up. The geometry and dimensions of the tensile specimen are taken from Sprave and Menzel (2020) and are specified in Fig. 4(a), showing total dimensions of 52 mm length, 10 mm width and 1.5 mm thickness. To reduce computational costs for the training of the GPR surrogate model, only one eighth of the specimen is simulated due to symmetry considerations and isotropic material response. Additionally applied Dirichlet boundary conditions to the symmetry planes ensure that symmetry conditions are met. To be specific, the small cross section within the y-z symmetry plane at $x = 0$ mm is constrained in x-direction, see Fig. 4(b). On the opposite side, the specimen is quasi-statically loaded by prescribing a monotonically increasing tensile displacement u_x, while the displacements in the y and z directions remain unconstrained at this boundary. The bottom x-z symmetry plane at $y = 0$ mm remains fixed in y-direction, whereas the x-y symmetry plane at $z = 0$ mm is fixed in the z-direction.

A mesh convergence study is conducted to motivate a computationally efficient and sufficiently accurate spatial discretization. The results in the form of force–displacement curves, see Fig. 5(a), are based on the reference material parameter set of DP800 steel, taken from Sprave and Menzel (2020), see Table 1, and a prescribed maximum tensile displacement of $u_x = 2$ mm. In addition, force–displacement curves for the identified upper and lower bounds material parameter sets are also highlighted; see also Fig. 11(f) in Appendix. Spatial discretizations of $n_{el} \in \{980, 2120, 4224, 8000, 16128\}$ number of elements are investigated using eight-noded trilinear hexahedral elements with full integration, which are additionally enhanced by an F-bar formulation to reduce non-physical (numerical) stiffening effects related to volumetric locking. The corresponding force–displacement curves in Fig. 5(a) show an initially mesh-independent response. With increasing load, the reaction force saturates and then shows a drop in reaction force starting at $u_x \approx 1$ mm for the reference material parameter set due to necking observed in the center region of the specimen. Deformation, respectively strain eventually localizes in one single element row, as also reflected by the proportional hardening related internal variable; see Fig. 5(b). This generally results in mesh-dependent solutions that necessitate a regularization technique applied to plasticity. Such a regularization approach is outside the scope of this contribution. For further background on modeling and simulation frameworks including regularization based on gradient contributions of plasticity-related quantities see, e.g., Kaiser and Menzel (2019a,b) and references cited therein. Moreover, gradient-based regularization of plasticity and damage contributions is discussed in Friedlein et al. (2023). For the subsequent variance-based global sensitivity analysis, respectively training of the GPR surrogate model, loading is reduced to a maximum tensile displacement of $u_x = 0.65$ mm to ensure that necking and, in consequence, mesh-dependent effects are avoided in the considered loading range — particularly for varying sets

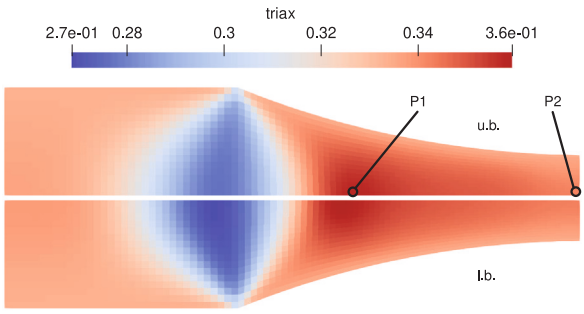

(a) Contour plots of stress triaxiality η by element average values at reduced tensile loading of $u_x = 0.65$ mm.

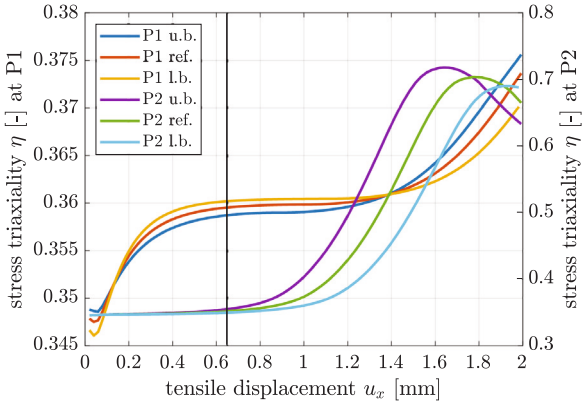

(b) Loading history of stress triaxiality η over tensile displ. for full loading of $u_x = 2$ mm evaluated at quadrature points P1 and P2.

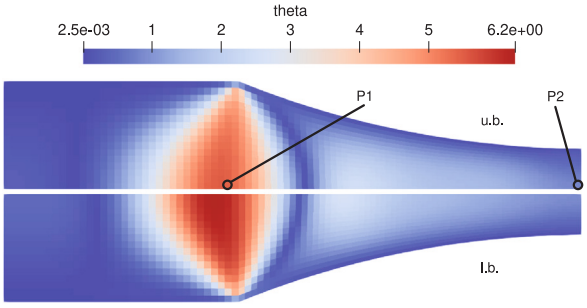

(c) Contour plots of Lode angle ϑ by element average values at reduced tensile loading of $u_x = 0.65$ mm.

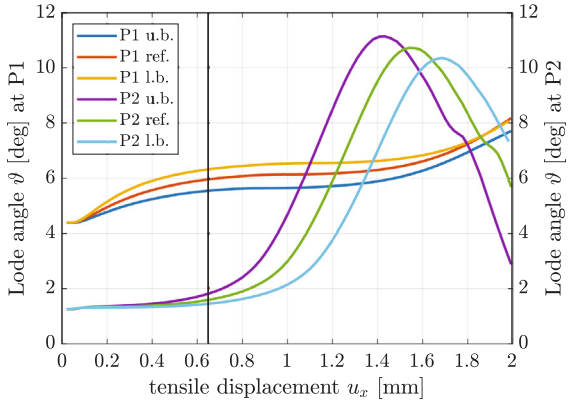

(d) Loading history of Lode angle ϑ over tensile displ. for full loading of $u_x = 2$ mm evaluated at quadrature points P1 and P2.

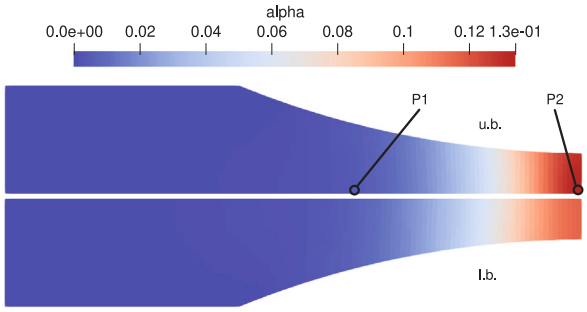

(e) Contour plots of hardening variable α by element average values at reduced tensile loading of $u_x = 0.65$ mm.

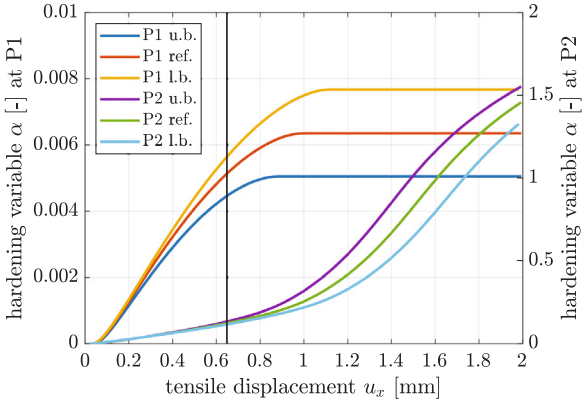

(f) Loading history of hardening variable α over tensile displ. for full loading of $u_x = 2$ mm evaluated at quadrature points P1 and P2.

Fig. 6. Contour plots and loading histories of stress triaxiality η, Lode angle ϑ and proportional hardening variable α over tensile displacement for $n_{el} = 8000$, evaluated for reference (ref.), upper bounds (u.b.) and lower bounds (l.b.) material parameter sets.

of material parameters analyzed for the training of the GPR surrogate model. A mesh convergence analysis based on reaction force history, as well as maximum stress triaxiality and Lode angle as integral and local convergence measures, results in a reasonable spatial discretization of $n_{el} = 8000$ elements, as depicted in Figs. 4(b) and 5(b).

In Figs. 6(a), 6(c) and 6(e) contour plots of η, ϑ and α are shown for the loading level $u_x = 0.65$ mm, which corresponds to the loading stage before necking as also considered within the uncertainty analysis as this work proceeds. Moreover, Figs. 6(b), 6(d) and 6(f) highlight graphs of η, ϑ and α at two selected positions of the specimen, whereby loading levels up to $u_x = 2$ mm are considered in order to qualitatively indicate the values and evolution of these quantities towards and within the necking stage of loading. As discussed in Appendix, the values of stress triaxiality and Lode angle are independent of the material

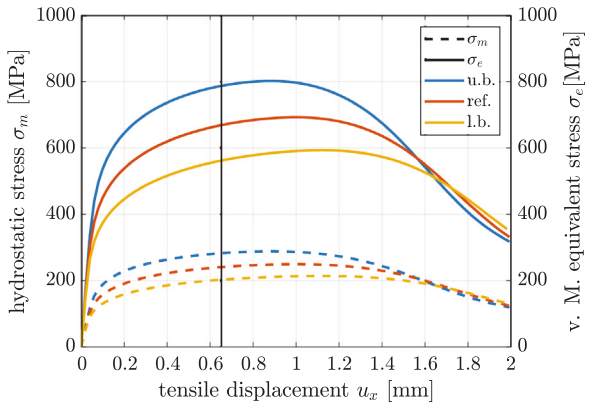

(a) Loading histories of hydrostatic stress σ_m and von Mises equivalent stress σ_e at quadrature point P1.

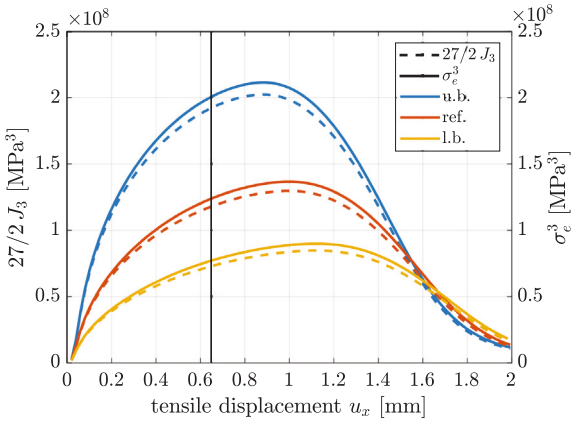

(b) Loading histories of second and weighted third (deviatoric) invariants J_2 and J_3 at quadrature point P1.

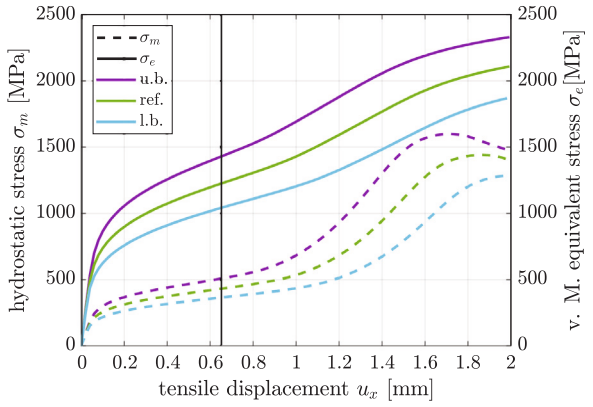

(c) Loading histories of hydrostatic stress σ_m and von Mises equivalent stress σ_e at quadrature point P2.

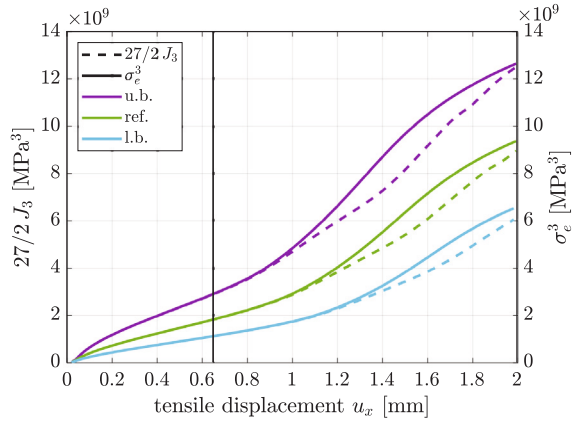

(d) Loading histories of second and weighted third (deviatoric) invariants J_2 and J_3 at quadrature point P2.

Fig. 7. Loading histories of hydrostatic stress σ_m, von Mises equivalent stress σ_e, as well as second and weighted third (deviatoric) invariants J_2 (here represented via σ_e^3) and J_3 over tensile displacement for full loading $u_x = 2$ mm at quadrature points P1 and P2 evaluated for reference (ref.), upper bounds (u.b.) and lower bounds (l.b.) material parameter sets.

parameter set in case of uniaxial tension, i.e. $\eta = 1/3$ and $\zeta = 1$ for $\boldsymbol{\sigma} = \sigma_{\parallel}\, \boldsymbol{e}_{\parallel} \otimes \boldsymbol{e}_{\parallel}$. The results shown in Figs. 6(a) and 6(c) reveal moderate values close to, but different from, those obtained for the stress state of uniaxial tension, cf. Table 5. Hence, an influence of material parameters on damage initiation indicators of stress triaxiality and Lode angle is expected. Both contour plots of stress triaxiality and Lode angle for upper and lower bounds material parameter sets show almost homogeneous results towards the center of the specimen and in the outer region of clamping with stress states much closer to uniaxial tension. In the center region, element average values of $\eta \approx 0.340$ and $\vartheta \approx 1.0°$ are observed for both material parameter sets. In contrast, in the clamping region, especially at the outer sides, values of nearly perfect uniaxial tension of $\eta \approx 0.333$ and $\vartheta \approx 0°$ are obtained. In turn, inhomogeneous results are observed in the transition zone from the specimen radius towards the clamping region, where overall maximum stress triaxiality and Lode angle are found on the middle axis of the specimen taking maximum element average values of $\eta \approx 0.358$ and $\vartheta \approx 5.5°$ for the upper bounds material parameter set and $\eta \approx 0.360$ and $\vartheta \approx 6.3°$ for the lower bounds material parameter set. The contour plots for the two material parameter sets mainly differ in magnitude, with the lower bounds material parameter set showing the highest maximum values. Only a minor shift in the location of maximum values is observed.

In Figs. 6(b) and 6(d), the loading histories of stress triaxiality and Lode angle evaluated on the Gauss point level over a tensile displacement of up to $u_x = 2$ mm are provided for two representative quadrature points denoted as P1 and P2, as well as for the three material parameter sets, as defined in Table 1. The quadrature point P1 denotes the integration points identified to show maximum values for stress triaxiality and Lode angle at the end of a reduced maximum tensile displacement of $u_x = 0.65$ mm, which is also used for the subsequent training of the GPR surrogate model. For most material parameter sets at this loading, the identified integration points P1 coincide with a fixed location for each damage initiation measure taking the positions indicated in Figs. 6(a) and 6(c). Otherwise, a quadrature point in the immediate proximity of P1 showing maximum values is identified and is used for training instead. The representative quadrature point P2 corresponds to one of the integration points of the element closest to the center of the specimen that exhibits the highest stress triaxiality and Lode angle values over the entire loading of up to $u_x = 2$ mm. The identified integration point P2 of that element, see Figs. 6(a) and 6(c), is fixed over the entire loading history.

Figs. 6(b) and 6(d) illustrate that non-trivial loading histories of stress triaxiality and Lode angle over tensile displacement are obtained at quadrature point P1. Starting from initial values close to those identified for the stress state of uniaxial tension, both damage initiation indicators of stress triaxiality and Lode angle increase towards a plateau, stay approximately constant and increase again at the end of loading while showing overall moderate values. At quadrature point P1, the lower bounds material parameter set generally results in the highest

stress triaxiality and Lode angle values, which agrees with results obtained from contour plots, cf. Figs. 6(a) and 6(c). More precisely, for stress triaxiality, the opposite applies to the increase in value at the beginning and at the end of loading, where, in turn, the upper bounds material parameter set results in the highest stress triaxiality values. Comparing results obtained for the force–displacement curves, see Fig. 5(a), it can be concluded that at quadrature point P1, the lowest reaction force curve generally results in the highest stress triaxiality, respectively Lode angle. The loading history of the proportional hardening related internal variable at quadrature point P1 highlighted in Fig. 6(f) shows that the hardening variable saturates to a constant, here in comparison, vanishingly small value. The saturation observed with increasing tensile loading is attributed to geometrically induced stress concentrations in the center region of the specimen, leading to a reduction in the load-bearing cross-sectional area, as shown in (Fig. 5(b)) and ultimately necking, as previously discussed. By increasing material parameters, the necking effect becomes more pronounced due to an increase in the evolution of plasticity, respectively proportional hardening variable; see Fig. 6(e). As a result, the outer regions of the specimen unload during increasing loading, effectively reducing the driving force of plasticity and therefore yielding smaller proportional hardening variable values at quadrature point P1 for the upper bounds material parameter set, as seen in Fig. 6(f).

Fig. 7 highlights graphs of σ_m, σ_e as well as of combinations of J_2 and J_3 by analogy with Figs. 6(b), 6(d) and 6(f). In particular, Fig. 7(a) depicts the loading histories of the hydrostatic stress and von Mises equivalent stress for different material parameter sets at quadrature point P1, which also show an unloading behavior as a result of necking once a critical maximum tensile displacement is surpassed. Taking the fraction of both measures results in stress triaxiality, as defined in Eq. $(10)_3$. Therefore, in combination, both curves motivate the loading history of stress triaxiality of Fig. 6(b) and explain how changes in material parameter sets influence stress triaxiality. For instance, the von Mises equivalent stress σ_e shows a higher decrease rate for the upper bounds material parameter set for increasing loads,which is a result of increased plastic unloading, leading to a comparatively higher stress triaxiality towards the end of loading, see Fig. 7(a), cf. Fig. 6(b). In analogy, following the stress mode factor parametrization in terms of $\zeta(J_3, \sigma_e)$, cf. Eq. $(11)_1$, Fig. 7(b) motivates the loading history of the Lode angle, where the numerator and the denominator are plotted against each other at the quadrature point P1. Both terms of $27/2\, J_3$ and σ_e^3 also show a decrease in values at different rates during necking, respectively plastic unloading, and motivate the loading history of the Lode angle of Fig. 6(d) over the tensile displacement at quadrature point P1.

Quadrature point P2, in turn, shows values for stress triaxiality and Lode angle before the onset of necking, which are slightly smaller, respectively significantly smaller than those obtained for quadrature point P1, see Figs. 6(b) and 6(d). With increasing tensile loading, stress triaxiality and Lode angle surpass their respective maximum values at quadrature point P1 and further increase towards high maximum values of $\eta \approx 0.7$ and $\vartheta \approx 11°$. Thereafter, a significant reduction in both measures is observed. As a result, maximum stress triaxiality and Lode angle switch between quadrature point P1 and P2 over the entire loading history. The decrease in stress triaxiality can be motivated by the plots of hydrostatic stress and von Mises equivalent stress evaluated at quadrature point P2 over the entire loading history, see Fig. 7(c). As loading increases and necking becomes dominant, the von Mises equivalent stress increase rate is approximately constant. In contrast, the hydrostatic stress shows a negative increase rate towards the end of loading, resulting in a decrease in stress triaxiality, cf. Eq. $(10)_3$. The reduction in Lode angle towards the end of loading at quadrature point P2, respectively the re-increase in stress mode factor, is analyzed via Fig. 7(d) using the alternative parametrization of the stress mode factor, cf. Eq. $(11)_1$. This shows that at the end of loading the increase rate of the weighted third deviatoric stress invariant $27/2\, J_3$ is higher than that of the von Mises equivalent stress to the power of three σ_e^3 due to a decrease in slope towards the end of loading in the latter quantity, which results in an increase in stress mode factor, respectively decrease in Lode angle.

In contrast to quadrature point P1, P2 generally shows the highest stress triaxiality, Lode angle and proportional hardening variable values for the upper bounds material parameter set throughout the loading, where variations regarding different material parameter sets are much more pronounced. The proportional hardening variable continuously increases towards high values, resulting in a necking behavior at increasing loadings, cf. Fig. 6(f). The results indicate that higher material parameter values are detrimental regarding damage initiation and evolution for high loading. For reduced loading, the opposite is observed. In view of higher maximum tensile displacements of $u_x > 1$ mm accompanied by necking, such investigations need to be re-evaluated in future work for results obtained by, e.g., gradient-based regularization of plasticity, which enables the quantification of the effect of uncertainty at high loading.

4.2. Results

In this section, the simulation framework for the quantification of the effect of uncertainty of material parameters on extremal stress triaxiality and Lode angle values is established by combining the nonlinear finite element model of an exemplary boundary value problem of a tensile test specimen introduced in Section 4.1 and the variance-based global sensitivity framework outlined in Section 3.

To this end, two GPR surrogate models for maximum stress triaxiality and Lode angle are trained separately. An initial batch of $n_d = 60$ training data points, i.e. sets of material parameters, is generated through Latin hypercube sampling assuming uniform distributions with lower and upper bounds defined in Table 1, which forms the basis for training both GPR surrogate models. To avoid loading into necking and therefore the necessity of a regularization technique applied to plasticity, as discussed in Section 4.1, the tensile test specimen is loaded up to a maximum tensile displacement of $u_x = 0.65$ mm. Therefore, maximum damage initiation indicators of stress triaxiality and Lode angle are evaluated at the quadrature point P1, as indicated in Figs. 6(a) and 6(c). To reduce numerical cost involved in finite element analyses, only one eighth of the specimen is simulated. A spatial discretization of $n_{\text{el}} = 8000$ number of elements is chosen based on the performed mesh convergence study in Section 4.1. As an additional remark, it should be noted that the initial set of $n_d = 60$ training data points was evaluated taking advantage of parallel computing. In this context, please note that the computation of each of these training data points is completely independent from the others. The evaluation of maximum triaxiality and Lode angle for different realizations of material parameters can be done in parallel by running several instances of the finite element model on available CPU cores simultaneously. This corresponds to the so-called *embarrassingly parallel case*, see e.g. Pellissetti (2009). While the relationship between computation time and the number of available cores is not linear, the parallel execution of simulations optimizes overall resource utilization by efficiently distributing the workload. Then, using this training data, each of the trained GPR models is used to produce estimates of the Sobol' indices associated with maximum stress triaxiality and Lode angle through the Bayesian probabilistic integration approach described in Section 3.5.2. The quality of these estimators is judged by calculating the coefficient of variation associated with each of the variances involved in the calculation of Sobol' indices, as described in Eqs. (16) and (17). More specifically, an estimator is deemed as accurate whenever the value of the coefficient of variation associated with each estimated variance (that involves the ratio between the standard deviation of the estimator and the expected value of the estimator) is below 10%. In case such criterion is not fulfilled, active learning is implemented in order to improve the quality of the GPR surrogate model. Following this active learning

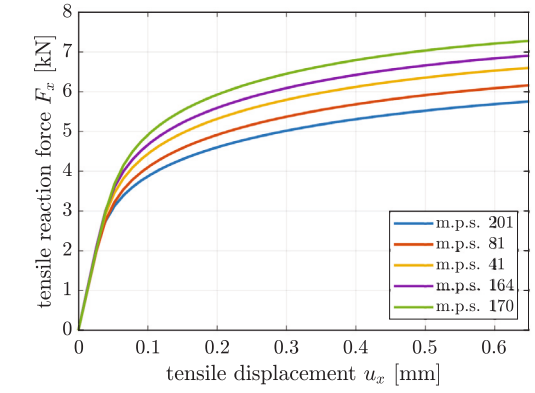

(a) Force-displacement curves.

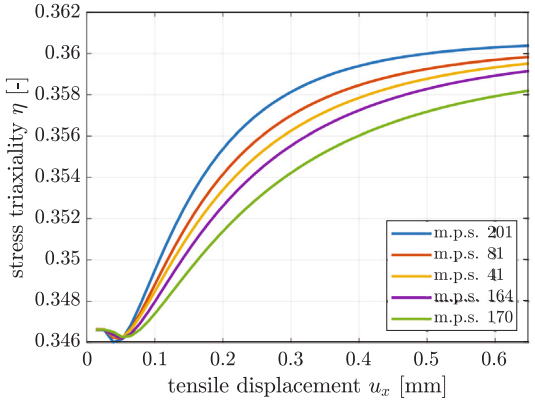

(b) Loading history of stress triaxiality η.

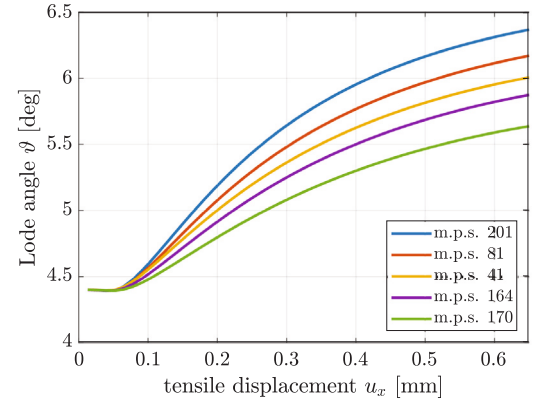

(c) Loading history of Lode angle ϑ.

Fig. 8. Force–displacement curves and loading histories of stress triaxiality η and Lode angle ϑ at quadrature point P1 for representative material parameter sets generated during training for reduced loading of $u_x = 0.65$ mm.

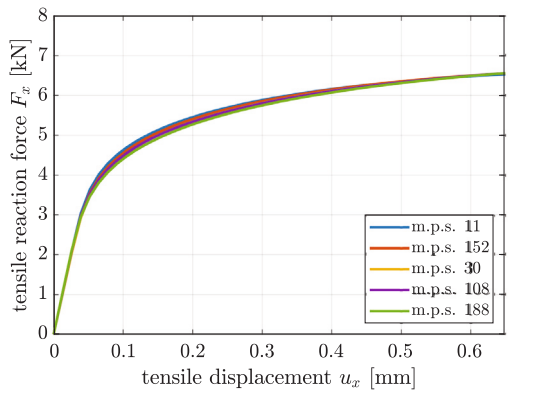

(a) Force-displacement curves.

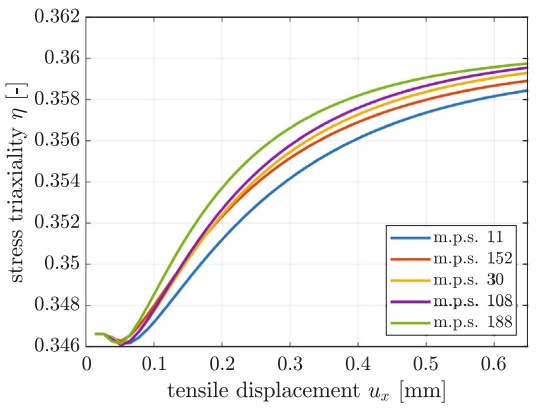

(b) Loading history of stress triaxiality η.

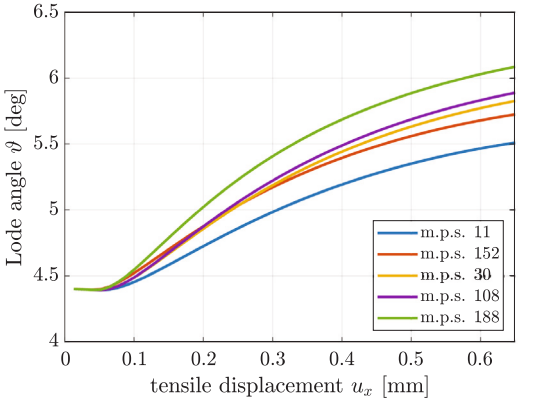

(c) Loading history of Lode angle ϑ.

Fig. 9. Force–displacement curves and loading histories of stress triaxiality η and Lode angle ϑ at quadrature point P1 for selected material parameter sets generated during training for reduced loading of $u_x = 0.65$ mm.

strategy, the GPR model associated with the stress triaxiality demanded performing 145 additional nonlinear finite analysis, while the GPR model associated with Lode angle demanded 66 additional analyses. As a side remark, it should be noted that active learning was implemented using a sequential approach that does not admit parallel computations. This is a consequence of the fact that each of the training data points identified through active learning depends on the training history of the GPR surrogate model.

Before analyzing the Sobol' indices estimated through the procedure described previously, it is of interest to have a closer look at results obtained for some of the training data points generated during the training of the GPR surrogate model. For that purpose, Figs. 8 and 9 illustrate the evolution of the tensile reaction force, stress triaxiality and Lode angle as a function of the tensile boundary displacement for different combinations of material parameters. More specifically, Fig. 8 illustrates the aforementioned quantities for the first five material parameter sets (m.p.s.) shown in Table 2. The selection of these parameters was deliberate and intended to capture the entire range of values observed for stress triaxiality and Lode angle, making them *representative* despite not being chosen at random. It is noted from Figs. 8(a), 8(b) and 8(c) that there is considerable variability between

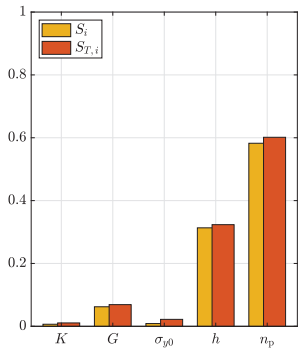

(a) First-order and total order Sobol' sensitivity indices S_i and $S_{T,i}$ associated with maximum stress triaxiality η.

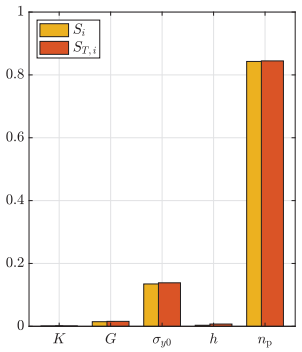

(b) First-order and total order Sobol' sensitivity indices S_i and $S_{T,i}$ associated with maximum Lode angle ϑ.

Fig. 10. Visualization of first-order and total order Sobol' sensitivity indices S_i and $S_{T,i}$ associated with maximum stress triaxiality η and Lode angle ϑ. Illustration of most influential material parameters and interaction effects identified by differences in first-order and total order Sobol' sensitivity indices.

Table 2
Representative material parameter sets as part of initial batch before active training and generated during active training.

	K [GPa]	G [GPa]	σ_{y0} [MPa]	h [MPa]	n_p [−]
m.p.s. 201	120.04	87.92	230.50	1575.63	0.2915
m.p.s. 81	119.90	82.22	233.80	1671.09	0.2803
m.p.s. 41	121.78	86.10	239.03	1742.87	0.2643
m.p.s. 164	114.52	88.46	254.03	1791.30	0.2586
m.p.s. 170	115.80	84.65	264.01	1844.13	0.2468
m.p.s. 11	115.74	88.15	267.84	1575.33	0.2426
m.p.s. 152	120.08	86.84	229.48	1643.19	0.2401
m.p.s. 30	118.59	84.58	259.86	1676.22	0.2614
m.p.s. 108	116.07	88.04	265.91	1683.35	0.2662
m.p.s. 188	118.25	88.77	249.00	1747.20	0.2731

Table 3
First-order and total Sobol' sensitivity indices of stress triaxiality before active learning for different n_d and after convergence.

n_d	S_K [−]	S_G [−]	$S_{\sigma_{y0}}$ [−]	S_h [−]	S_{n_p} [−]
10	0.0000	0.1394	0.0000	0.3586	0.4857
60	0.0185	0.0530	0.0075	0.3125	0.5682
60 + 145	0.0065	0.0622	0.0087	0.3134	0.5825
	$S_{T,K}$ [−]	$S_{T,G}$ [−]	$S_{T,\sigma_{y0}}$ [−]	$S_{T,h}$ [−]	S_{T,n_p} [−]
10	0.0000	0.1550	0.0000	0.3721	0.5027
60	0.0322	0.0662	0.0134	0.3403	0.5980
60 + 145	0.0107	0.0690	0.0221	0.3234	0.6015

Table 4
First-order and total Sobol' sensitivity indices of Lode angle before active learning for different n_d and after convergence.

n_d	S_K [−]	S_G [−]	$S_{\sigma_{y0}}$ [−]	S_h [−]	S_{n_p} [−]
10	0.0000	0.0069	0.1337	0.0000	0.8451
60	0.0007	0.0143	0.1283	0.0043	0.8389
60 + 66	0.0006	0.0146	0.1348	0.0033	0.8428
	$S_{T,K}$ [−]	$S_{T,G}$ [−]	$S_{T,\sigma_{y0}}$ [−]	$S_{T,h}$ [−]	S_{T,n_p} [−]
10	0.0000	0.0076	0.1456	0.0000	0.8564
60	0.0010	0.0166	0.1335	0.0088	0.8449
60 + 66	0.0008	0.0157	0.1384	0.0072	0.8445

the maximum values of tensile force, stress triaxiality and Lode angle for different realizations of the material parameter sets, respectively. These findings are in agreement with results obtained in Section 4.1, where for the highest reaction force curves, the lowest stress triaxiality and Lode angle values are obtained. Upon closer inspection of the material parameter sets arranged by maximum stress triaxiality value in Table 2, it is noteworthy that the table entries are ordered perfectly by yield stress σ_{y0}, hardening modulus h, and hardening exponent n_p. This unintentional result provides an initial indication of the material parameters that may have the greatest influence on stress triaxiality and Lode angle. However, it does not provide information about the relative magnitudes of these effects, nor does it account for possible interactions among the parameters, which is considered to be of utmost importance in this study. Meanwhile, Fig. 9 illustrates tensile force, stress triaxiality and Lode angle for the last five material parameter sets (m.p.s.) shown in Table 2. These sets of parameters are labeled as *selected*, as they were chosen such that the maximum tensile force values exhibit almost no variability, as observed in Fig. 9(a). Remarkably, Figs. 9(b) and 9(c) show that there is still considerable variability between the maximum values of stress triaxiality and Lode angle for different realizations of these selected material parameter sets. Such behavior reveals the inherently complex relation between the uncertain material parameters and the responses of interest. Thus, when conducting tensile test specimens when calibrating material parameters, close attention must be paid to these complexities.

In a next step, the Sobol' indices associated with stress triaxiality and Lode angle are analyzed. Table 3 and Fig. 10(a) report the estimated Sobol' indices associated with stress triaxiality while Table 4 and Fig. 10(b) report the Sobol' indices associated with Lode angle. Several important conclusions can be drawn from these tables and figures, as discussed in detail below.

- Both Tables 3 and 4 report the estimated indices for different numbers of training data points, namely $n_d = 10$ (that is, considering a subset of the data generated with Latin Hypercube sampling), $n_d = 60$ (data generated with Latin Hypercube sampling) and $n_d = 60 + 145$ or $n_d = 60 + 66$ (data generated with Latin Hypercube sampling and active learning). It is observed that even with $n_d = 10$ data points, it is possible to generate rough estimates of the Sobol' indices. The additional simulations over $n_d = 10$ contribute mostly to refine the estimates of the indices, particularly for those that possess a small numerical value.
- Figs. 10(a) and 10(b) show that the first-order and total order Sobol' indices are almost identical, while verifying that $S_i \leq S_{T,i}$. This reveals that for the problem at hand, the effect of uncertainty on material parameters on stress triaxiality and Lode angle is of additive nature.
- The results reported in Appendix and Section 4.1 suggested that material parameters governing plasticity may possess a considerable impact on stress triaxiality and Lode angle.
- The Sobol' indices associated with stress triaxiality (see Fig. 10(a)) indicate that the most relevant material parameters are the hardening exponent n_p, the hardening modulus h and the shear modulus G. In contrast, for the case of the Lode angle (see Fig. 10(b)), only the hardening exponent n_p and the yield stress σ_{y0} are

relevant, with the hardening exponent n_p playing the more preponderant role. Such differences in the number of relevant parameters may explain the difference observed regarding the number of training data points in Tables 3 and 4. Indeed, less data points may be required in the case of the Lode angle (a total of 126 nonlinear finite element analyses) because there is one parameter (the hardening exponent) that almost completely dictates all the variability.

As a summary of the above observations, it is noted that Sobol' indices offers an excellent means for performing a quantitative sensitivity analysis that allows learning much about the input–output relations of challenging engineering models.

5. Summary and outlook

In this work, a variance-based global sensitivity analysis framework was proposed that allows for an efficient quantification of uncertainty effects of material parameters characterizing elasto-plasticity on stress triaxiality and Lode angle.

Several relevant conclusions can be drawn from the strategies and results presented in this work. From a purely algorithmic viewpoint, it has been shown that a state-of-the-art numerical model for characterizing the behavior of a mechanical device can be effectively interfaced with algorithms for uncertainty quantification. In this regard, the application of a surrogate model plays a pivotal role. Indeed, the Gaussian process regression (GPR) model considered in this work is trained with a moderate number of nonlinear finite element analysis. Once this GPR is trained, it is possible to perform uncertainty quantification at reduced numerical costs. Furthermore, the active learning strategy implemented in this work allows to improve the quality of the GPR surrogate gradually with a limited number of additional nonlinear finite element analyses. This is quite remarkable, as active learning allows to enrich the initial training set (generated with Latin hypercube sampling) such that the uncertainty associated with the estimation of probabilistic descriptors is minimized. From the point of view of the results presented, sensitivity analysis allows performing a quantitative assessment of the problem at hand, which is most relevant from a practical viewpoint. In fact, the results presented in Fig. 11, which involve a simple sensitivity study, already indicated that the material parameters governing plasticity affect the most the maximum stress triaxiality and Lode angle, respectively. While such results as discussed in Appendix are certainly valuable, they are intrinsically qualitative. On the contrary, the Sobol' indices as reported in Section 4.2 provide quantitative evidence, revealing that most of the variability present in both stress triaxiality and Lode angle can be attributed to the variability associated with the hardening exponent n_p. Such quantitative evidence suggests that to better control stress triaxiality and Lode angle (and eventually damage), it is necessary to pay close attention to this hardening exponent. This observation is reinforced by the results obtained for selected material parameter sets during GPR surrogate model training, where notable differences in stress triaxiality and Lode angle were found despite showing nearly identical force–displacement curves (the latter typically being considered for classic calibration of material parameters). For example, one could attempt to identify more precisely the range of uncertainty of this exponent by combining prior knowledge on it plus practical laboratory measurements under the framework provided by Bayesian updating.

The computational framework established in the present work contributes to the simulation-based prediction of the influence of uncertainty of material parameters on process-induced material properties. The particular application analyzed emphasizes evolution of stress triaxiality and Lode angle in the context of finite deformation elasto-plasticity since these contributions are typical indicators for damage evolution and thereby for the material properties influenced, respectively induced, by the underlying manufacturing process. Such type of analysis becomes (in future) most important in view of processing impure raw materials with high uncertainties in initial material properties – e.g. in the context of saving resources by means of recycling materials or making use of scrap metal in manufacturing processes. Moreover, the current contribution provides a basis for continuing investigations and expansions of the established framework. Further developments could involve exploring the nonlinear finite element model of the tensile test specimen under increased loadings, aiming to quantify uncertainty effects of material parameters near the onset of necking, where a change in the influence of material parameters on stress triaxiality and Lode angle has been observed. The highly mesh-dependent results obtained in the current implementation towards necking suggest that an extension of the framework by a regularization technique applied to plasticity is required, resulting in the solution of, e.g., an additional non-local proportional hardening-related internal variable field alongside the displacement field. Furthermore, extending the current framework by a damage formulation would enable a more comprehensive analysis of uncertainty effects associated with material parameters that govern the initiation and evolution of damage in the tested specimen.

Several more sophisticated tensile test specimens are found in the literature that are designed to provoke different stress states, which can be adopted into the current framework to investigate the effects of uncertainty of material parameters at varying levels of stress triaxiality and Lode angle. Moreover, by considering non-uniform spatially distributed sets of material parameters, a more realistic analysis can be achieved, which closely resembles the behavior observed in real-life applications.

Another venue for improving the numerical performance of the implemented framework for sensitivity analysis consists of exploiting parallel process capabilities. From a general perspective, approaches for uncertainty quantification are usually highly parallelizable, as they comprise repeated evaluation of a deterministic model. However, for the current problem at hand, parallelization is not straightforward to implement in context with an active learning scheme. Henceforth, specific research in this area is required in order to further improve the numerical properties of the implemented scheme.

Declaration of competing interest

The authors declare that they have no known competing financial interests or personal relationships that could have appeared to influence the work reported in this paper.

Data availability

Data will be made available on request.

Acknowledgments

Financial support by the Deutsche Forschungsgemeinschaft (DFG, German Research Foundation) – Project-ID 278868966 – TRR188 is gratefully acknowledged.

Appendix. Homogeneous uniaxial tension

In order to illustrate the influence of the material parameters of the material model discussed in Section 2.2, homogeneous states of deformation under uniaxial tension are investigated with respect to a reference material parameter set that was fitted to DP800 steel, taken from Sprave and Menzel (2020), see Table 1, and variations thereof. In order to illustrate the main characteristics and properties of the material model itself, also extreme values for the underlying materials parameters are considered in the following, which are not representative for DP800 steel as represented by the reference set of material parameters; cf. Table 1.

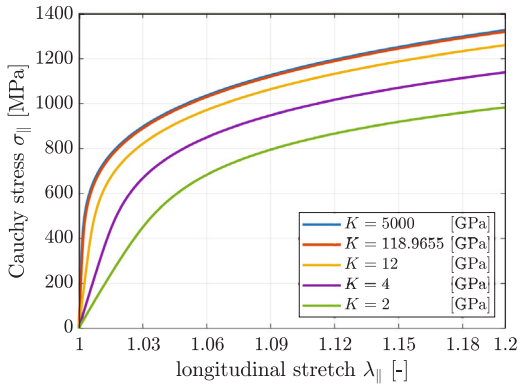

(a) Influence of the bulk modulus K.

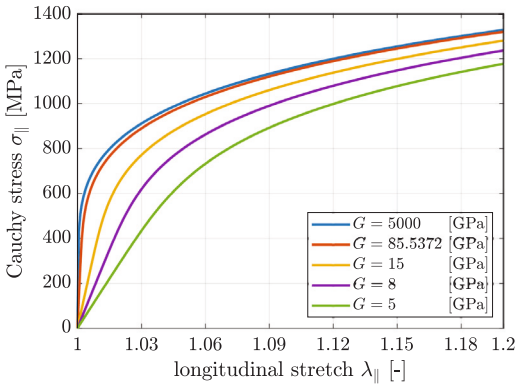

(b) Influence of the shear modulus G.

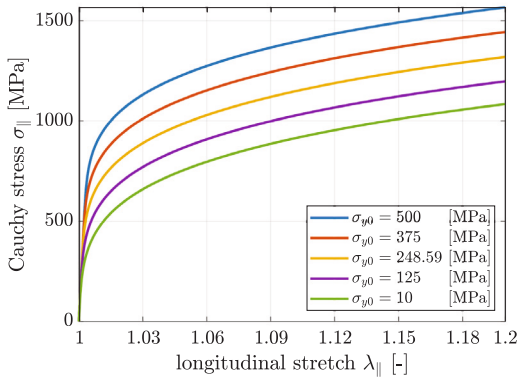

(c) Influence of the yield stress σ_{y0}.

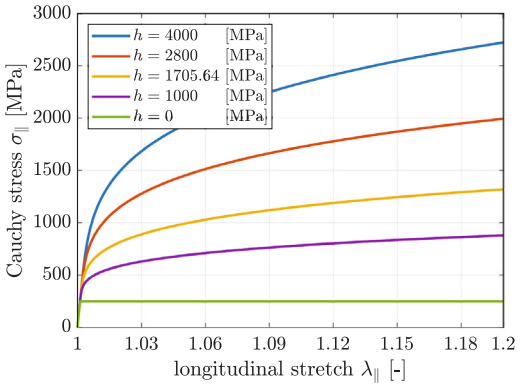

(d) Influence of the hardening modulus h.

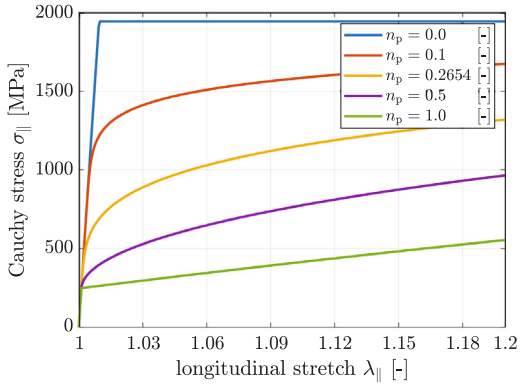

(e) Influence of the hardening exponent n_{p}.

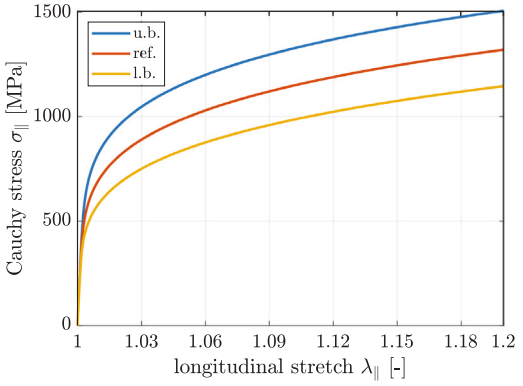

(f) Results for material parameter sets defined in Table 1.

Fig. 11. Influence of the variation of material parameters on the constitutive response in the form of stress–stretch curves obtained for homogeneous states of deformation under uniaxial tension. Comparison against the reference material parameter set.

For an isotropic material response, the deformation gradient (related to a uniaxial stress state) takes the form

$$\boldsymbol{F} = \lambda_{\parallel}\, \boldsymbol{e}_{\parallel} \otimes \boldsymbol{e}_{\parallel} + \lambda_{\perp} \left[\boldsymbol{I} - \boldsymbol{e}_{\parallel} \otimes \boldsymbol{e}_{\parallel} \right], \tag{19}$$

wherein $\lambda_{\parallel}$ denotes the prescribed monotonically increasing stretch in longitudinal tension direction $\boldsymbol{e}_{\parallel}$ with $\|\boldsymbol{e}_{\parallel}\| = 1$. The stretch $\lambda_{\perp}$ results from the constraint of a uniaxial tension stress state, i.e. $\boldsymbol{\sigma} = \sigma_{\parallel}\, \boldsymbol{e}_{\parallel} \otimes \boldsymbol{e}_{\parallel}$, with $\sigma_{\parallel}$ being the Cauchy stress in longitudinal tension direction.

In Fig. 11, the material response of the reference material parameter set in terms of stress–stretch curves of the uniaxial Cauchy stress $\sigma_{\parallel}$ over the longitudinal stretch $\lambda_{\parallel} \in [1.0, 1.2]$ is compared against the material response obtained for material parameter variations where one of the parameters is varied at a time. The graphs illustrate that the material parameters governing plasticity exert the most significant influence on the constitutive behavior in the vicinity of the reference material parameter set. The bulk and shear moduli K and G significantly influence the stress–strain response already before yielding; see Figs. 11(a) and 11(b). However, this is the case only for high variations of their reference values, whereby higher values result in higher stresses. The latter is not expected to occur in practice. Varying yield stresses σ_{y0}, see Fig. 11(c), shows distinct trends already for comparatively small variations. Thereby, the elastic and plastic regimes are clearly distinguishable by the onset of yielding. It is observed that the curves take a parallel path with a constant offset in the plastic regime, where the offset is directly related to the difference in yield

Table 5
Stress triaxiality η and stress mode factor ζ evaluation for different stress states with principal Cauchy stresses σ_1, σ_2, σ_3.

	$\sigma_1 > 0$ $\sigma_2 = \sigma_1$ $\sigma_3 = \sigma_1$	$\sigma_1 > 0$ $\sigma_2 = \sigma_1$ $\sigma_3 = 0$	$\sigma_1 > 0$ $\sigma_2 = 0$ $\sigma_3 = \sigma_2$	$\sigma_1 > 0$ $\sigma_2 = -\sigma_1/2$ $\sigma_3 = \sigma_2$	$\sigma_1 > 0$ $\sigma_2 = 0$ $\sigma_3 = -\sigma_1$	$\sigma_1 > 0$ $\sigma_2 = \sigma_1$ $\sigma_3 = -2\sigma_1$	$\sigma_1 = 0$ $\sigma_2 = \sigma_1$ $\sigma_3 < 0$	$\sigma_1 = 0$ $\sigma_2 < 0$ $\sigma_3 = \sigma_2$	$\sigma_1 < 0$ $\sigma_2 = \sigma_1$ $\sigma_3 = \sigma_1$
η	∞	2/3	1/3	0	0	0	−1/3	−2/3	$-\infty$
ζ	∞	−1	1	1	0	−1	−1	1	$-\infty$

stresses. The hardening modulus h, see Fig. 11(d), significantly influences the hardening evolution after yielding in terms of the magnitude of the stress–stretch curve, whereby a vanishing hardening modulus results in perfect plasticity. Finally, the hardening exponent defines the nonlinearity of the hardening evolution with $n_p = 1$ resulting in linear hardening and $n_p = 0$ resulting in perfect plasticity, see Fig. 11(e). In contrast to the other material parameters, the hardening exponent shows a decrease in stresses for increasing values. The resulting stress–stretch curves for the reference, upper and lower bounds material parameter sets defined in Table 1 are provided in Fig. 11(f) for comparison. Based on the discussed results obtained for varying hardening exponents, the upper bounds material parameter set contains the lowest hardening exponent, and the opposite applies to the lower bounds parameter set, with overall ±5% and ±10% variations of elastic and plastic material parameters with respect to the reference material parameter set.

The respective values of stress triaxiality and Lode angle for a stress state of uniaxial tension are constant over the entire loading history of $\eta = 1/3$ and $\vartheta = 0°$, respectively $\zeta = 1$, cf. Table 5 with principal Cauchy stresses σ_1, σ_2, σ_3 of type $\sigma_1 > 0$, $\sigma_2 = 0$ and $\sigma_3 = \sigma_2$. In particular, stress triaxiality and Lode angle are independent of the set of material parameters for the stress states shown.

References

Bai, Y., Wierzbicki, T., 2008. A new model of metal plasticity and fracture with pressure and lode dependence. Int. J. Plast. 24, 1071–1096. http://dx.doi.org/10.1016/j.ijplas.2007.09.004.

Banabic, D., 2010. Sheet Metal Forming Processes. Springer Berlin, Heidelberg, http://dx.doi.org/10.1007/978-3-540-88113-1.

Briol, F.X., Oates, C.J., Girolami, M., Osborne, M.A., Sejdinovic, D., 2019. Probabilistic integration: A role in statistical computation? Statist. Sci. 34, 1–22. http://dx.doi.org/10.1214/18-STS660.

Brünig, M., Gerke, S., Hagenbrock, V., 2013. Micro-mechanical studies on the effect of the stress triaxiality and the Lode parameter on ductile damage. Int. J. Plast. 50, 49–65. http://dx.doi.org/10.1016/j.ijplas.2013.03.012.

Darlet, A., Desmorat, R., 2015. Stress triaxiality and Lode angle along surfaces of elastoplastic structures. Int. J. Solids Struct. 67–68, 71–83. http://dx.doi.org/10.1016/j.ijsolstr.2015.03.006.

Davis, E.A., Connelly, F.M., 1959. Stress distribution and plastic deformation in rotating cylinders of strain-hardening material. J. Appl. Mech. 26, 25–30. http://dx.doi.org/10.1115/1.4011918.

Elnashai, A.S., Chryssanthopoulos, M., 1991. Effect of random material variability on seismic design parameters of steel frames. Earthq. Eng. Struct. Dyn. 20, 101–114. http://dx.doi.org/10.1002/eqe.4290200202.

Faes, M.G., Daub, M., Marelli, S., Patelli, E., Beer, M., 2021. Engineering analysis with probability boxes: A review on computational methods. Struct. Saf. 93, 102092. http://dx.doi.org/10.1016/j.strusafe.2021.102092.

Faravelli, L., 1989. Response-surface approach for reliability analysis. J. Eng. Mech. 115, 2763–2781. http://dx.doi.org/10.1061/(ASCE)0733-9399(1989)115:12(2763).

Fishman, G.S., 1996. Monte Carlo: Concepts, Algorithms and Applications. Springer, New York, NY, http://dx.doi.org/10.1007/978-1-4757-2553-7.

Friedlein, J., Mergheim, J., Steinmann, P., 2023. Efficient gradient enhancements for plasticity with ductile damage in the logarithmic strain space. Eur. J. Mech. A/Solids 99, 104946. http://dx.doi.org/10.1016/j.euromechsol.2023.104946.

Hurtado, J.E., Alvarez, D.A., 2001. Neural-network-based reliability analysis: A comparative study. Comput. Methods Appl. Mech. Engrg. 191, 113–132. http://dx.doi.org/10.1016/S0045-7825(01)00248-1.

Jones, D.R., Schonlau, M., Welch, W.J., 1998. Efficient global optimization of expensive black-box functions. J. Global Optim. 13, 455–492. http://dx.doi.org/10.1023/A:1008306431147.

Kaiser, T., Menzel, A., 2019a. A dislocation density tensor-based crystal plasticity framework. J. Mech. Phys. Solids 131, 276–302. http://dx.doi.org/10.1016/j.jmps.2019.05.019.

Kaiser, T., Menzel, A., 2019b. An incompatibility tensor-based gradient plasticity formulation—theory and numerics. Comput. Methods Appl. Mech. Eng. 345, 671–700. http://dx.doi.org/10.1016/j.cma.2018.11.013.

Lemaitre, J., 1996. A Course on Damage Mechanics, second ed. Springer Berlin, Heidelberg, http://dx.doi.org/10.1007/978-3-642-18255-6.

Lode, W., 1926. Versuche über den einflußder mittleren hauptspannung auf das fließen der metalle eisen, kupfer und nickel. Z. Phys. 36, 913–939. http://dx.doi.org/10.1007/BF01400222.

Malcher, L., Andrade Pires, F.M., César de Sá, J.M.A., 2012. An assessment of isotropic constitutive models for ductile fracture under high and low stress triaxiality. Int. J. Plast. 30–31, 81–115. http://dx.doi.org/10.1016/j.ijplas.2011.10.005.

Malcher, L., Mamiya, E.N., 2014. An improved damage evolution law based on continuum damage mechanics and its dependence on both stress triaxiality and the third invariant. Int. J. Plast. 56, 232–261. http://dx.doi.org/10.1016/j.ijplas.2014.01.002.

McKay, M.D., Conover, W.J., Beckman, R.J., 1979. A comparison of three methods for selecting values of input variables in the analysis of output from a computer code. Technometrics 21, 239–245. http://dx.doi.org/10.2307/1268522.

Mediavilla, J., Peerlings, R.H.J., Geers, M.G.D., 2006. A nonlocal triaxiality-dependent ductile damage model for finite strain plasticity. Comput. Methods Appl. Mech. Eng. 195, 4617–4634. http://dx.doi.org/10.1016/j.cma.2005.10.001.

Murakami, S., 2012. Continuum damage mechanics. In: Solid Mechanics and Its Applications, Vol. 185. Springer Dordrecht, http://dx.doi.org/10.1007/978-94-007-2666-6.

Oakley, D.R., Sues, R.H., Rhodes, G., 1998. Performance optimization of multidisciplinary mechanical systems subject to uncertainties. Prob. Eng. Mech. 13, 15–26. http://dx.doi.org/10.1016/S0266-8920(97)00004-0.

Patelli, E., Pradlwarter, H.J., Schuëller, G.I., 2010. Global sensitivity of structural variability by random sampling. Comput. Phys. Comm. 181, 2072–2081. http://dx.doi.org/10.1016/j.cpc.2010.08.007.

Pellissetti, M., 2009. Parallel processing in structural reliability. J. Struct. Eng. Mech. 32, 95–126.

Rasmussen, C.E., Williams, C.K.I., 2006. Gaussian Processes for Machine Learning. MIT Press, http://dx.doi.org/10.7551/mitpress/3206.001.0001.

Saltelli, A., Ratto, M., Andres, T., Campolongo, F., Cariboni, J., Gatelli, D., Saisana, M., Tarantola, S., 2008. Global Sensitivity Analysis: The Primer. John Wiley & Sons, http://dx.doi.org/10.1002/9780470725184.

Simo, J.C., 1998. Numerical analysis and simulation of plasticity. In: Numerical Methods for Solids (Part 3) Numerical Methods for Fluids (Part 1). In: Handbook of Numerical Analysis, vol. 6, Elsevier, pp. 183–499. http://dx.doi.org/10.1016/S1570-8659(98)80009-4.

Sivia, D.S., 1996. Data Analysis - a Bayesian Tutorial. Oxford University Press, New York.

Sobol', I.M., 1993. Sensitivity estimates for nonlinear mathematical models. Math. Model. Comput. Exp. 1, 407–414.

Song, J., Wei, P., Valdebenito, M.A., Faes, M., Beer, M., 2022. Data-driven and active learning of variance-based sensitivity indices with Bayesian probabilistic integration. Mech. Syst. Signal Process. 163, 108106. http://dx.doi.org/10.1016/j.ymssp.2021.108106.

Sprave, L., Menzel, A., 2020. A large strain gradient-enhanced ductile damage model – finite element formulation, experiment and parameter identification. Acta Mech. 231, 5159–5192. http://dx.doi.org/10.1007/s00707-020-02786-5.

Sprave, L., Schowtjak, A., Meya, R., Clausmeyer, T., Tekkaya, A.E., Menzel, A., 2020. On mesh dependencies in finite-element-based damage prediction: application to sheet metal bending. Prod. Eng. 14, 123–134. http://dx.doi.org/10.1007/s11740-019-00937-9.

Sudret, B., 2008. Global sensitivity analysis using polynomial chaos expansions. Reliab. Eng. Syst. Saf. 93, 964–979. http://dx.doi.org/10.1016/j.ress.2007.04.002.

Zhu, Y., Engelhardt, M.D., 2018. A nonlocal triaxiality and shear dependent continuum damage model for finite strain elastoplasticity. Eur. J. Mech. A/Solids 71, 16–33. http://dx.doi.org/10.1016/j.euromechsol.2018.03.012.